

The Effect of Storms on the 1992 Summer Sea Ice Cover of the Beaufort,
Chukchi and East Siberian Seas

Benjamin Holt

Seelye Martin¹

Mail Stop 300-323, Jet Propulsion Laboratory, California Institute of Technology
4800 Oak Grove Drive, Pasadena, CA 91109

1. School of Oceanography, Box 357940,
University of Washington, Seattle WA 98195-9740

ben@pacific.jpl.nasa.gov

• seelye@ocean.washington.edu

Short Title: Storms and the Summer Ice Cover

Submitted to

Journal of Geophysical Research Oceans

15 October 1999

Abstract

For the summer Beaufort, Chukchi and East Siberian Seas, a variety of passive and active microwave data is used to determine the response of the ice edge and interior to a storm. Specifically, the study concentrates on a low-pressure system which passed over the region between 14 - 20 August 1992, with peak geostrophic winds of about 18 m s^{-1} . Through the use of the Special Sensor Microwave/Imager (SSM/I) data and the 100-km wide ERS-1 radar swaths, we examine the ice edge response at a nearly stationary location in the Chukchi Sea, and in the ice interior along three swaths in the Beaufort and Chukchi Seas, and in the East Siberian Sea north of Wrangel Island. The ice edge observations show that the storm fractures the large floes into small floes, some of which are advected into the adjacent warm water. The ice interior observations show that the storm caused an increase in the open water amount, and a shift in the floe size distribution toward smaller floes. Application of the cumulative number distribution $N(d)$ in the ice interior, where N is the number of floes per unit area which are no smaller than some floe diameter d , shows that for $d > 1 \text{ km}$, N behaves like $d^{-\alpha}$, where α lies in the range 1.8 - 2.9. We also find that the slope is unchanged by the storm, and that it is slightly larger near the ice edge.

1. Introduction

In the summer Beaufort, Chukchi and East Siberian Seas (Figure 1), at least three factors determine how ice melts. The first is the advection of warm water by ocean currents toward the ice edge. In our region of interest, the major source of warm water is the northward flow of warm water through the Bering Strait into the Chukchi Sea. This flow divides into three parts: the Alaskan Coastal Current, the westward flow of warm water through DeLong Strait between Wrangel Island and Siberia, and the northward flux of warm water through a topographic depression east of Wrangel Island [*Coachman et al.*, 1975; *Martin and Drucker*, 1997]. The second factor is the summer onset of warm weather and the seasonal peak in the solar radiation, which heats the water surrounding the floes, causing surface and side wall melting [*Maykut and Perovich*, 1987]. Given this source of melt, the third factor determining the melt rate is the regional distribution of floe sizes. The importance of this distribution is that in warm water, ice floes melt from above and below, but most importantly from the sides [*Steele*, 1992]. Given that small floes have a larger ratio of perimeter to upper surface area than large floes, small floes melt more quickly than large ones.

Given that small floes tend to melt away in summer, the question remains, how does the floe size distribution change over the summer, and in particular, how does it change before and after a storm? In the present paper, we discuss in our sector of interest, how this distribution is in part determined and maintained by the passage of summer storms, which occur at an approximately monthly basis. Because the strong winds create shear fields within the ice, and ocean swell in the open water adjacent to the ice, the flexural cracking and floe abrasion induced by these swell and shear fields break the large floes into many small floes. This qualitative argument suggests that the storms provide a source of small floes, while the ice melting provides a sink, with the difference going into a reduction in ice extent.

Because of the difficulties in the determination of floe size distributions from aircraft and satellite imagery, studies of these distributions are relatively rare. *Vinje* [1977] used LANDSAT imagery to measure only those floes greater than $10 \times 10 \text{ km}^2$ passing through Fram Strait and found that there was a decrease in the number of all floe sizes during early summer. *Hall and Rothrock* [1987] measured lateral melt using aerial photography, finding melt rates as high as 10 cm per day or 1 m over 10 days, which is too small to measure with current satellite imagery.

Rothrock and Thorndike [1984, hereafter *RT-84*] also examine the floe size distribution from three aerial photographic mosaics and one LANDSAT image taken on either different dates or at different locations, and from a separate analysis by *Weeks et al.* [1980], then discuss the properties of the summer floe size distribution. In their analysis, they use the cumulative number distribution $N(d)$, where d is a measure of the floe diameter, and $N(d)$ is the number of floes per unit area with diameters greater than d . Their image analysis shows that for $0.1 \text{ km} < d < 100 \text{ km}$, $N(d)$ decreases approximately as $d^{-\alpha}$, where α lies in the range $1.7 < \alpha < 2.5$. *RT-84* feel that $N(d)$ is the most informative of the floe statistics they investigated. They also show that this power law behavior is approximately correct, but has a slightly steeper slope for larger floes, changing to a more gradual slope for smaller floes. The importance of the power law dependence is that “floes of a fixed size ratio occur in numbers of a fixed ratio [*RT-84*, page 6480]”, so that the floe distributions are self-similar, and as *RT-84* illustrate, images of collections of floes at different scales tend to look the same.

In the following, we investigate how a summer storm affects the pack ice. In particular, we examine the specific role of an August 1992 storm in the determination of the ice edge position, and of the ice interior properties. In the ice interior, we will show that the storms cause an increase in the amount of open water within the pack, and they appear to fracture large floes into small ones. At the ice edge, the storms also generate small floes, where some of these are advected by ice edge eddies into the adjacent warm

water to melt. However, comparison of the large-scale position before, during and after the storm suggests that the storm had a negligible effect on the ice retreat.

In the following, Section 2 summarizes the data used in the study, Section 3 describes the large-scale response of the ice edge to the storm, and Section 4 describes the small-scale response of the ice edge. Then, Section 5 gives the general backscatter properties of the ice, and describes our method for retrieval of ice concentration and floe size distribution from the SAR imagery. Section 6 describes our results from the ice interior including the changes in the interior open water and floe size distributions, and shows that our floe statistics are similar in behavior to those observed by *RT-84*. Section 7 gives our conclusions.

2. The data used in the study

In the following, we determine the large scale behavior of the summer ice edge using the daily Special Sensor Microwave/Imager (SSM/I) passive microwave data set, which provides regional distributions of brightness temperatures at a resolution of 25-50 km. We determine the smaller scale ice properties from the VV-polarized ERS-1 C-band (5.3 GHz) Synthetic Aperture Radar (SAR) imagery, which provides image strips along 100 km wide swaths at approximately 3-day intervals. Finally, we derive the regional surface pressure fields from the 12-hour gridded NCEP (National Center for Environmental Prediction) data set.

Because in summer, the ice surface is often partially covered by liquid water and with many liquid water clouds present above the ice, the water vapor sensitive 37-GHz channel cannot be used in the ice retrievals [*Cavalieri et al.*, 1984]. Instead, following *Martin and Drucker* [1997], we determine the ice edge position using only the 19-GHz polarization ratio Pr :

$$Pr = \frac{19V - 19H}{19V + 19H} \quad (1)$$

where the 19V and H refers to the vertically and horizontally polarized 19-GHz channels. Because even in summer, Pr is sensitive to the contrast between open water and sea ice, we define the ice edge as the $Pr = 0.16$ threshold, where values greater than this are open water, and values smaller are ice. The spatial accuracy of this retrieval is determined by the 50-km diameter of the 19-GHz field-of-view.

Within the pack, we determine the floe size distributions and the open water area from the ERS-1 SAR imagery. During the 1992 summer, the satellite was in a 35-day orbital repeat cycle with both 3-day and 9-day near-repeat sub-cycles. The data were received, processed, and calibrated by the Alaska SAR Facility (ASF). Figure 1 shows the location of the rectangular strips which contain the 100-km wide swaths within the ASF mask, these swaths include coverage in the Beaufort Sea north of Point Barrow, the central Chukchi Sea, and the East Siberian Sea north of Wrangel Island. Each swath is made up of image frames measuring $100 \times 100 \text{ km}^2$, with adjacent frames overlapping by about 10%, and is obtained in strips or data takes of up to 2000 km in length. Although the SAR data is available at 25-m resolution, to reduce the radar speckle, we use intermediate resolution data averaged to 100-m pixels, which means that we could not observe the very small diameter (30 m) rapidly-melting floes considered by *Steele* [1992].

3. The large-scale ice and meteorological behavior

For our region of interest, we next briefly describe the regional weather and ice behavior during the 1992 summer, with particular emphasis on the August storm. For June through September 1992, Figure 2 shows the magnitude and direction of the geostrophic winds in the central Chukchi Sea, where we use geostrophic winds because they are approximately parallel to the ice drift. If we define a storm as an event with geostrophic wind speeds greater than 10 m s^{-1} , then such events occur at approximately monthly intervals. Examination of the surface pressure fields contained in the reports of the International Arctic Buoy Program [Ignatius Rigor, Applied Physics Laboratory, University of Washington, Seattle WA 98105-6698, and <http://iabp.apl.washington.edu/>]

shows that this storm frequency is consistent with other years. Also, *Maslanik et al.* [1996] shows that in spite of the large increases in the number of storms north of Siberia since 1989, in our Chukchi-Beaufort region of interest, the amount of cyclone activity for April-September, 1982-1993 has remained roughly constant, so that 1992 should be a fairly representative year.

Figure 2 also shows that the strongest sustained winds occur between 14 and 20 August. To expand on this storm, Figure 3 shows the sequence of regional daily surface pressure charts for the period 7 - 21 August. On about 14 August, a low pressure system appears in the northern East Siberian Sea at about 80°N , then moves east, remaining over the region until about 18 August. As it moves, it generates strong westerly and southwesterly winds in the East Siberian, Chukchi and Beaufort Seas.

For comparison with the winds, and for the same period, Figure 4 shows the ice edge location derived from three day averages of the SSM/I-derived ice edge, where the center day of each average corresponds to one of the SAR images given below. In the Chukchi Sea, the rectangular frame outlines a box which contains the SAR imagery; the winds in Figure 2 are from the center of this box. The figure shows that the ice edge extends from the Alaskan coast across the Chukchi Sea to Wrangel Island, then into the East Siberian Sea, where it turns to the north at about 168°E . Because the mean winds over the entire region and period are primarily from the west, the general ice drift is toward the east. In the Chukchi Sea, and particularly in the eastern half of the frame, the ice edge is advected to the northeast, where the largest displacements occur following the average edges for 7 and 13 August, where these displacements are in response to southwest geostrophic winds.

4. The SAR ice edge properties

The fine scale response of the ice edge is shown by examination of SAR images taken between 8 and 21 August, where these images are taken well after the previous period of strong winds ending on 21 July (Figure 2). Figure 5 gives the images; the rectangle containing each image corresponds to the box in Figure 4. Figure 5a is taken on 8 August

before the storm during a period of on-ice winds, where these winds generate waves incident on the ice edge, which because of wave herding of any loose floes against the edge and possible wave breaking at the edge creates the observed sharp and in places bright ice edge. The image also shows that immediately to the north of the edge, the pack consists of an apparently solid sheet of pack ice crossed by pressure ridges with no indication of separate floes.

Following 8 August, the surface pressure charts show that by 11 August, northwest off-ice winds occur over the image rectangle. Comparison of the 11 August image in Figure 5b with 5a shows that the 11 August image is located slightly more to the west than 8 August, the feature X which is common to both images has drifted slightly to the east, and the off-ice winds are associated with a large increase in the size of the diffuse ice edge region. Examination of the pack ice southwest of X in Figure 5b suggests that in the three day period, about 20 km of previously solid ice adjacent to the edge has been fractured into small floes.

After 11 August, the wind velocities increase from the northwest, shifting to a westerly flow on 14 August. Comparison of the 14 August image in Figure 5c with 5b shows that the common feature Y has also drifted to the east, and that the region of diffuse ice southwest of Y has greatly expanded in area. Within this region of diffuse floes, there is also a suggestion of ice floes being advected away from the edge by an ocean eddy.

Between 14 and 17 August, the storm dominates the winds, with peak winds on 15 August, advecting the ice to the southeast. On 17 August, the winds are reduced from their peak, but remain large and westerly. For 17 August, Figure 5d shows a dramatic change in the ice appearance. At this time, almost the entire ice field consists of small broken floes separated from one another by water made bright by wind roughening. There are also no identifiable floes which can be used for comparison with previous images. Three days later on 20 August, the winds remain strong and as Figure 5e shows, the ice edge remains a mixture of large and diffuse small floes.

5. General backscatter properties of the pack ice

For the same weather conditions, we next examine the distribution of open water and floe sizes in the ice interior. We begin with a discussion of the general backscatter properties of summer ice and open water, then describe a binary scheme for classification of each image into ice and open water. We finally describe a different algorithm for the separation and retrieval of ice floes from each image, which we use to determine the floe size distribution.

For the ERS-1 SAR, which operates over a range of incidence angles of 20-26°, because of brine drainage and surface melting during the Arctic summer, first year ice is largely indistinguishable from multi-year ice, and the range of summer ice backscatter values is generally between -10 and -17 dB [*Winebrenner et al.*, 1994, 1996; *Comiso and Kwok*, 1996; *Barber et al.*, 1995]. The sources of this variability include changes in the distribution of melt ponds [*Barber et al.*, 1995; *Comiso and Kwok*, 1996], and the rapid temperature excursions above and below the freezing point which are common in late summer, affect the surface water phase, and may change the backscatter by several dB [*Winebrenner et al.*, 1996].

For the ERS-1 scatterometer, which uses the same electronics package as the SAR and operates over a range of incidence angles of about 18-55°, *Stoffelen and Anderson*, [1997] have derived the open water backscatter. Figure 6 gives the approximate range of backscatter from summer ice as a function of incidence angle [*Onstott*, 1992; *Winebrenner et al.*, 1994, 1996; *Comiso and Kwok*, 1996; *Barber et al.*, 1995] and open water values for two wind speeds and a range of incidence angles [*Stoffelen and Anderson*, 1997]. This figure shows the incidence angle dependence of the backscatter, and that the water backscatter additionally depends on wind speed. Over the ERS-1 SAR angles for backscatter from water and for wind speeds greater than $2\text{-}3\text{ m s}^{-1}$, which is the threshold speed necessary for appearance of Bragg scattering waves, we observe backscatter greater than -8 dB at all wind directions relative to the antenna beam over the ERS-1 SAR

incidence angle range. Conversely, wind speeds smaller than the Bragg threshold yield backscatter values less than -15 dB (not shown in Figure 6). For both ice and water, the backscatter has a strong incident angle dependence, which decreases with increasing angle, and with the open water backscatter having a steeper slope than sea ice.

5.1 Retrieval of the open water area

Given this backscatter dependence, we next describe a binary image analysis scheme for the classification of each scene into ice and open water. This procedure uses an algorithm that allows for the linear adjustment of the threshold between ice and open water as a function of incidence angle in 0.1 dB steps [Comiso and Kwok, 1996]. A side-by-side comparison of the SAR image and the resultant ice/water binary image allows us to separate ice and open water with an accuracy of about 10%. Also, as Figure 6 shows, for the ERS-1 range of incidence angles and for wind speeds greater than $2\text{--}3\text{ m s}^{-1}$, open water is generally brighter than ice. However, for a few images, open water is brighter than ice at the smallest angles, but becomes darker with increasing angles. In these cases, open water was measured separately on each half of the image and then added together into one measurement for the entire scene. Finally, although along a swath, each scene overlaps with its neighbors by about 10%, we did not remove this overlap from the ice concentration results, which adds some uncertainty to the absolute concentration values between adjacent scenes but has minimal impact on the trends.

In the ice interior and under strong wind conditions, the division into ice and open water was generally straightforward, since the wind-roughened open water between floes is uniformly brighter than the surrounding ice. The algorithm works less well when the winds are weak, yielding low backscatter from water which reduces the contrast with the surrounding ice. Also, a large extent of dark ice without leads yields poor results. In the marginal ice zone (MIZ) however, the situation is more complicated because the large differences in the local wind and ice conditions result in a highly variable backscatter, which makes it difficult for the algorithm to work. Another complication in the MIZ is

the presence of other backscatter sources, such as ocean circulation features, biological slicks, and the presence of grease ice or of mixtures of slush and small ice floes; each of which either does not occur, or has less impact in smaller, narrower leads. These multiple factors make it difficult for the algorithm to work near the ice edge.

In the interior, certain summer ice conditions also contribute to the measurement uncertainty. The presence of wind-roughened ice surface melt ponds may result in an overestimation of the open water amount [Comiso and Kwok, 1996]; however, this factor is seasonally dependent, since the number of ponds generally decreases as summer progresses. Second, if sub-resolution ice floes, or floes with diameters smaller than the 100-m pixel scale, are present in the leads, we may interpret ice floes as open water. Another complication is that the exposed edge of a floe presents a vertical surface which may create a bright area resembling open wind-roughened open water and yield a slight overestimate of the open water area.

5.2 Determination of the floe size distribution

In our determination of the floe size distribution, we use an image analysis algorithm based on the restricted growing concept that enables us to separate objects while maintaining the object size [Soh *et al.*, 1998]. This approach finds floes that have a definitive shape and size, shrinks them to provide separation between adjacent floes, then returns them to their original shape and size while maintaining separation. This approach has significant advantages in retaining the original shape and size of the floes, even for floes as small as a few pixels, and in being relatively automatic as compared with the related approaches for floe identification such as Banfield and Raftery [1992] and Korsnes [1993].

Our application of the Soh *et al.* [1998] floe algorithm has the following steps:

- 1) Image enhancement, where to reduce speckle, the image is first processed with a moving 3 by 3 pixel median filter. This results in objects which are locally homogeneous while retaining their higher contrast edges.

2) Image segmentation, which consists of a technique called local dynamic thresholding [Haverkamp *et al.*, 1995]. This uses a set of user-specified thresholds to divide the image into floes, open water, and a water/ice mixture which we call 'substrate' and consists of sub-pixel sized floes in a mixture of brash and water. This technique works best when the floes have a low backscatter and the open water has a large, wind-roughened backscatter.

3) Floe extraction, which uses the restricted growing concept to identify distinct and separable floes.

4) Floe shape filtering, which eliminates those floes identified in the previous step which are not sufficiently compact. These include floes which appear overly elongated or branchy, where these floes result from the program's inability to find a clear separation between adjacent floes at their point of contact. This separation can be improved through use of a contrast enhancement technique described below. We classify this category of low confidence, filtered floes as 'discarded'.

5) Determination of the floe size distribution, which provides a count of the number of pixels in each floe identified by and retained in the previous steps.

In summary, application of this procedure combined with the open water algorithm described in Section 5.1 results in four classifications: open water, substrate, floes with irregular shapes which are discarded, and floes with regular shapes. [We note that the floe algorithm also produces an open water classification but it is not accurate and is mentioned here for completeness only. Instead we use the algorithm for open water described in Section 5.1].

As described in *Soh et al.* [1998], in some cases, the number of discarded floes increased at larger incident angles, due primarily to the reduced contrast between ice and ocean at the larger angles. To reduce this dependency, we determine a linear fit of the mean image brightness to the incidence angle. Application of the inverse of this slope to the image provides a flattened brightness response across the image, which increases the

contrast between ice and water and improves the floe separation. Both the uncorrected and slope-corrected image are then run separately through the floe size algorithm, following which the output is visually inspected. This inspection considers both the accuracy of the measurements and whether the output captures the range of floe sizes present. In the latter case, if the algorithm accurately determines the presence of small floes, but not larger floes, which is generally due to difficulties with the floe separation, the image is not selected for further analysis. If both the uncorrected and slope corrected images are successful, the image with the largest fractional percentage of measured floes is used in the analysis. This slope-correction procedure often significantly reduces the percentage of discarded floes, which particularly affects larger floes, and increases the percentage of correctly identified floes as compared to the uncorrected image. Finally, we remove the 10% overlap from adjacent images along a swath, so that the floe size statistics will be independent.

Table 1 lists the imagery used in the study, where for each swath, the first column shows the orbit number, and the second and third columns show the center latitudes and longitudes for the first and last images along the swath,. The fourth and fifth column show the time and date of each swath. The last four columns show the total number of frames or images in the swath, and the number of successful images as a function of three latitude bands. Examination of these columns and their totals shows that successful floe size measurements are obtained in roughly 50% of the analyzed frames. Of these successful results, over half were derived from slope-corrected images.

For the successful images, Table 2 gives the range of pixels contained in the sixteen size categories into which we group the observed floe sizes, which we describe in terms of pixels and km^2 , and in terms of the derived floe diameters. Specifically and for each category, the first column lists the class number, and the second column lists the range of the number of pixels, where successive categories contain approximately double the number of pixels. The third and fourth columns list the mean area in both pixels and km^2 ,

and the fifth column lists the mean caliper diameter d , defined from *RT-84*. For an arbitrary floe, they define the caliper diameter as the distance between two parallel lines where each line touches one side of the floe without penetrating the floe interior. *RT-84* derive the relation between d and the floe area A from examination of 782 floes in the AIDJEX summer mosaic, and find that on average, $A = 0.66d^2$. We use this relation to calculate d from the mean floe area.

To illustrate the floe classification procedure, Figure 7 shows the input SAR image (7a) which in this case is not slope-corrected, the output color classified into the different size classes (7b), and a histogram (7c) showing the percentage area covered by each of the following four classes: ice floes, discarded floes, substrate, and open water. This shows that the substrate is the largest class, followed by the regular floes. Finally, the lower right figure (7d) shows the fractional area covered by the different floe size classes seen in (7b).

In Figure 7, the substrate area is derived by subtraction of the areas of the open water and the two floe categories (floes and discarded) from the entire image. In general, we found that substrate was the single largest category, exceeded only by open water in a few cases, with substrate concentration values ranging from 20-40%. Because the algorithm does not work very well for floe diameters less than about 0.5 km, we are unable to use the substrate as an analog to determine the fate of the smallest floes.

The ability of the floe algorithm to derive accurate floe sizes primarily depends on environmental factors and on how these factors affect the backscatter as well as the nature of the ice pack [Soh *et al.*, 1998]. The algorithm works best when the floes are visually discrete, have a uniformly dark backscatter due to surface wetness, and are in high contrast with the bright wind-roughened leads and/or the interstitial ice. In cases when a single large floe is made up of several smaller floes which are frozen together into a single aggregate, the algorithm may decompose this large floe into its component floes. This decomposition is more apparent earlier in the summer, since by late summer the interstitial ice has generally melted leaving behind the larger floes.

The difficulties with the floe algorithm are as follows. No attempt has been made to estimate the size of those floes that are not wholly contained within the scene. The primary impact of this on the results is an underestimate of the area of floes with diameters greater than 16 km. However, this problem is not considered significant in this study for the following two reasons: (1) large floes are not particularly prevalent in the study area and (2) our emphasis is primarily on smaller floe sizes. Another caveat concerns the 100-m pixel size and the restricted growing concept in the floe algorithm, which shrinks an object to improve separation with its neighboring objects and then grows the object back to its original size while maintaining the separation. Clearly dealing with small objects of a few pixels in size is problematic since shrinking is not meaningful in those cases. Given these two bounds on the small and large sizes and as our results will indicate, the floe size measurements are most reliable between classes 5-14 (440 m-10 km in diameter).

6. Results from the ice interior

This section describes our results in the ice interior, beginning with the changes in the open water distributions, continuing with the floe size distributions, and concluding with a comparison of our observed floe number statistics with those of *RT-84*.

6.1 Changes in the open water distributions

Using the binary algorithm described in Section 5.1, Figure 8 presents the total ice concentration plotted versus latitude and day for the three swath locations in Figure 1. Because the storm propagates from west to east, we first discuss the Wrangel swath, continuing with the Chukchi and Beaufort swaths.

For Wrangel, Figure 8a shows the ice concentration plotted versus latitude for 13, 16 and 22 August, where the swaths extend from about 71°N to 78°N. The pressure charts in Figure 3 show that the peak winds along this swath occur between 14 and 18 August. Also, the ice edge plots in Figure 4 show in the East Siberian Sea, that part of the edge extending to the north remains well away from the swath. Although because of ice advection, the swaths on different days probably do not include the same ice floes, Figure

8a shows a pattern in the ice behavior from before and after the storm. The August 13 curve from before the storm, shows the ice edge location, and that the ice concentration rises to about 100% within three frames of the edge. The August 16 curve, which is taken during the storm and has a swath length limited by data availability, shows that in the ice interior the concentrations have fallen to 90-95% between 75-78°N. Finally on August 22 or following the storm, the concentrations have fallen further to 75-85% between 76-78°N. This suggests that the storm passage has led to a reduction in the interior ice concentration.

For the Chukchi, Figure 8b shows seven concentration curves taken between 8 and 26 August. The curves show that there is a strong trend toward increasing open water along the swath with time. The meteorological data shows that the peak winds again occur during 14-18 August. Before the storm, the curves for 8, 11 and 14 August are nearly identical, with some ice reduction occurring near the edge, with a rise to a nearly 100% concentration in the interior. During the storm, the 17 August curve shows that the ice concentration decreased to 73% south of 75°N, while remaining large to the north. The 20 August curve shows a continued reduction in the ice concentrations (<95%) south of 79°N. Compared with 20 August, the 24 August curve shows a concentration increase at about 76°N; while the August 26 curve shows that the reduction in ice concentration begins south of about 81°N, with a significant reduction to about 65% at 79°N. To summarize in relation to the storm (August 14-20), before the storm there was little open water north of 73°N, while during and after the storm there was increasing open water within the entire pack including the steady progression northward (from 72°N to 76°N) of the region of extensive open water.

Finally, Figure 8c shows the five Beaufort ice concentration curves for 13-26 August. While this region experienced strong winds between 14 and 20 August, the figure shows that the ice interior did not respond greatly to the winds. For all figures, the ice concentrations north of 75.5°N remained consistently large, with the exception of a slight opening to 98% on August 19 and August 25 between 81-83 °N. South of 75.5°N, the

concentrations fluctuated, reaching their lowest values on August 25, then increasing again on August 26. In summary, during and following the storm, the ice interior remained intact, while the southerly portion become slightly less compact. North of 73°N, the ice concentrations were never less than 98%.

From these data sets, the effects of the storm are seen in the Wrangel and Chukchi swaths, where especially in the Chukchi, there is a steady increase in open water throughout the ice cover, with the largest openings at the highest latitudes occurring after the storm. Conversely, in the Beaufort Sea, the winds appear to make the ice more compact, and the storm-induced changes are much smaller than in the other regions. This difference between the Beaufort swath and the other swaths may be due to the large amount of open water near the coasts in the Wrangel and Chukchi cases.

6.2 The floe size distributions

Following *RT-84*, we next discuss the floe size distribution. For each image and the size ranges listed in Table 2, we define A_i as the area covered by floes of class i . We also define N_i as the number of floes in each class, where N_i equals A_i divided by the mean area of each class listed in Table 2. Given N_i , we can easily construct the previously discussed cumulative number distribution $N(d)$. In the following, we first discuss the behavior of N_i and A_i for the different swaths, then discuss the number distribution $N(d)$, where we show that our results compare well with *RT-84*.

6.2.1. Changes in the number and area of the floes as a function of floe size

As Table 1 and Figure 8 show, even though the ice concentration measurements extend further south, we were only able to obtain accurate floe size measurements between 72-83°N. For this latitude range, the last three columns in Table 1 list the number of frames with accurate measurements by swath within the latitude bands, 72-75°N, 75-78°N, 78-83°N. This shows that south of 75°N, Wrangel has 0, Chukchi 6, and Beaufort 10 frames with accurate measurements, while in the other two latitude groupings, the number of useful measurements is distributed more evenly. For the different swaths, we therefore

average N_i and A_i into these three latitude bands; and further into three time periods, 8-13 August, 14-20 August, and 21-26 August, corresponding to before, during and after the storm.

For the Wrangel swath, Figure 9a shows N_i plotted versus floe class for all available data, where floe measurements were obtained only north of 75°N , before August 14 and after August 21. The figure shows that most of the floes have diameters ranging from 0.4 to 3.4 km (classes 5-11), with a peak in the distribution between 0.9 – 1.2 km (classes 7-8). Also within each floe class following the storm, there is nearly a three-fold increase in the number of floes, compared with before the storm. For the same latitude bands and time periods, Figure 10a plots A_i versus floe class, and shows that there is a similar increase in the floe areas following the storm, except that for obvious reasons the distribution is now weighted toward larger floes.

For the Chukchi swath, Figure 9b shows that for all latitude bands, the peak in N_i again occurs at a diameter of about 1 km (class 8), and that the majority of floes have diameters between 0.4 and 3.4 km (classes 5-11). One difference compared with the Wrangel case is that in the Chukchi case for each latitude band, there are many more small floes. For 78°N – 83°N , even though there was no data available before the storm, comparison of the curve from during the storm with that following shows a shift toward smaller and fewer floes in the middle range of floe sizes (diameters 0.9 – 3.4 km; classes 7-11), and a decrease in the number of smaller floes. For 75°N – 78°N , the figure shows that after the storm passage, the number of floes in the mid-range classes increases slightly, while there is a small decrease in the number of small floes. For 72°N – 75°N , there is about a 50% reduction in the number of floes following the storm for all sizes up to 5 km diameter (class 12) plus a decrease in the peak of the distribution from 1.2 to 0.9 km (class 8 to 7). In summary, whereas for the Wrangel case, we observed more floes following the storm, for the Chukchi case, we observe the reverse.

For the corresponding Chukchi area distributions, Figure 10b shows that except for the smallest floes, the area covered by the different floe classes decreases. Comparison of these results with those of ice concentration (Figure 8b), shows that the large increase in open water at both the high and low latitude bands on August 26 coincides with a significant reduction in number of floes and area covered by floes in these regions.

Figures 9c and 10c show similar plots for the Beaufort swath. Examination of Figure 9c shows that as with the other swaths, most of the floe diameters are in the range 0.4 - 3.4 km (classes 5-11), and that the floe distribution again peaks at a diameter of about 1 km (class 8). For all three latitude bands, comparison of the distributions before and after the storm shows that there is a small shift toward smaller floes for diameters in the mid-sized range of 0.6 – 2.4 km (classes 6-10), and a reduction (although less pronounced than in the Chukchi) in the number of floes after the storm, particularly in the northern and southern latitude bands. The only increase in the number of smallest floes (class 1-4) occurs at the lowest latitude. Finally, examination of Figure 10c shows, with the exception of the largest floe class in the 78-83°N band, that the areal coverage remains nearly constant with time. At 78-83°N and after the storm, the figure shows that a few large floes make a significant contribution to area, where these floes were probably advected into the swath.

6.2.2. *The cumulative number distribution $N(d)$*

We next discuss the distribution of $N(d)$ for the various swaths, and compare it with RT-84. For each swath and for the latitude bands and the time periods used in Figures 9 and 10, Figure 11 shows $N(d)$ plotted versus d on a log-log scale. Each of the sub-figures show that the resultant curves divide into three parts: for $d < 0.9$ km (classes 1-6), the curves are nearly flat, which means that comparatively few floes occur in these categories; for $0.9 \text{ km} < d < 10 \text{ km}$ (classes 7-14), the curve has a negative, nearly- constant slope, and for $d > 10 \text{ km}$ (classes 15-16), where also only a few floes occur, the curves are sometimes steeper and sometimes less steep than the constant slope region. Further, with only a few exceptions, the curves tend to overlies each other. The exceptions include the

Wrangel plots, which show more floes after than before the storm, the 72-75°N Chukchi plot, where fewer small floes occur following the storm, and the 78-83°N Beaufort plot, where slightly more large floes occur following the storm.

For each swath, Table 3 lists for the constant slope portion of the cumulative number plots (diameter range $0.9 \text{ km} < d < 10 \text{ km}$), where the fall-off can be described by $d^{-\alpha}$, the values of α with their error for each latitude band and for the ranges of 72-83°N (total) and for 72-78°N (to match the approximate range of latitudes covered by the RT-84 AIDJEX analysis). The table shows that the values of α range from 1.9 to 2.9. For 72-78°N, we observe that $2.0 < \alpha < 2.7$, where this range is slightly larger but close to RT-84 results of $1.7 < \alpha < 2.5$. For the three latitude bands, our data also show a slight increase in α for 72-75°N, which is the latitude band closest to the ice edge. Averaged over all latitudes (72-83°N), the α range from 1.9 to 2.6, where the Wrangel and Chukchi slopes are generally steeper than the Beaufort case, inferring that the Beaufort case has more large floes than the other cases.

6.2.3. Comparison with RT-84

We now compare our values of $N(d)$ with RT-84 (their Figure 7). Their plot contains the following Arctic data: 1) An aerial photographic mosaic from the Arctic Ice Dynamics Joint Experiment (AIDJEX), 18 August 1975 [Hall, 1978], 2) A Landsat image, 185 x 155 km, 18 August 1973, 3) Four U-2 aerial photographs of areas about 30 km on a side, taken June 21, 1974, and 4) Two X-band airborne side-looking radar images taken on 23 September 1975 flying swaths north of Alaska [Weeks *et al.*, 1980, their figure 7]. Most of this data was taken during AIDJEX at a latitude of about 75°N; the Weeks *et al.* data was taken in the MIZ north of Barrow.

Figure 12a, the RT-84 results, show that the four data sets analyzed by RT-84 have similar trends. In contrast, the Weeks *et al.* [1980] curve is steeper and offset from the other curves, with an initial floe diameter of about 2 km, an overall α of about 2.5, and where the steepest part of its curve has $\alpha = 3.8$. The figure also shows as RT-84 observe,

that even though the two U-2 mosaics were taken on the same day 50 km apart, one of the U-2 curves is steeper than the other. Figure 12b shows our data superimposed on Figure 12a, using the mean of all values for each swath over the latitude range of 72-78°N. The figure shows that, even though the linear portion of our data has a slightly steeper slope, it overlies the *RT-84* data. Our curves are also clustered more tightly together, which may simply reflect that unlike *RT-84*, all our data was taken with the same instrument and during a narrower time period. Note that our results show the most similarity to the AIDJEX mosaic and Landsat results which were also taken during August. Also, the presence of the flat regime in our data simply reflects the lack of consistent ability of the SAR data and the algorithms to isolate floes below about 1 km. These results indicate several things. First, they provide a strong indication that between 1-10 km, our floe algorithm generates comparable results to previous measurements. Also, the wide variation seen in the previous data is not seen in our measurements, despite the impact of the storm, which suggests that some of the variation in the *RT-84* data is likely due to the different observational techniques as well as the different months and regions that are sampled.

7. Conclusions

The effect of a severe storm on the ice edge and interior properties of the Beaufort and Chukchi Seas are studied using a variety of remote sensing tools. For both the ice edge and interior, the work uses the ERS-1 SAR 100 km wide swaths, where these swaths drift slightly to the west over the period of interest. At the ice edge, the imagery shows that the storm fractures the adjacent large ice floes into many small floes, some of which are distributed by ocean eddies into the adjacent warm water. The overall ice edge advance and retreat however, appears to be qualitatively determined by the winds. In the ice interior, changes in the amount of open water appear to be greater in those regions which border on large areas of open water so that ice divergence can occur, such as the Chukchi and East Siberian Seas, with the largest changes occurring after the passage of the storm.

For the Beaufort Sea, probably because of the lack of nearby open water, there is no change in the ice interior concentration associated with the storm.

In the Chukchi and to a lesser extent in the Beaufort swaths and compared with conditions before the storm, there was a shift in floe size distribution toward smaller floes after the storm with a concomitant change in floe size area. The most pronounced changes in floe size distributions, either toward smaller floes as in the Chukchi and Beaufort track or increased number of floes as seen in the more sparsely sampled Wrangel track, are associated with areas of significantly reduced ice concentration.

From examination of the cumulative number distribution used by *RT-84*, we find that our distributions yield a power law behavior similar to theirs. Because of the 100-m pixel size, our ice floe algorithm cannot resolve floes reliably with diameters smaller than about 0.5 km diameter. This means that even though our ice edge analysis shows that the storm yields the production of small floes from large ones, the low resolution of our floe size algorithm only provides an indication rather than proof of this storm-related transition in the ice interior.

Acknowledgments

We acknowledge the support of NASA under Contract NAG5-4176 to the University of Washington and thank the Alaska SAR Facility (ASF) for providing us with the SAR data. We also thank the National Snow and Ice Data Center (NSIDC), in Boulder, CO for providing us with the SSM/I data. SM also thanks Robert Drucker for help with data processing. The JPL effort was supported by the National Aeronautics and Space Administration through a contract with the Jet Propulsion Laboratory, California Institute of Technology. BH also thanks Xiang Liu (JPL), Bruno Revelin and Pierre Leon who visited JPL on work-study programs through SUPAERO in Toulouse, as well as Leen-Kiat Soh of the University of Kansas. Publication number 0000, School of Oceanography, University of Washington.

References

- Coachman, L. K., K. Aagaard, and R. B. Tripp, *Bering Strait, The Regional Physical Oceanography*, University of Washington Press, Seattle, 172 pp., 1975.
- Banfield, J., and A. E. Raftery, Ice floe identification in satellite images using mathematical morphology and clustering about principal curves, *J. Am. Stat. Assoc.*, 87 (417), 7-16, 1992.
- Barber, D. G., T. N. Papakyriakou, E. F. LeDrew, and M. E. Shokr, An examination of the relationship between the spring period evolution of the scattering coefficient and energy fluxes over landfast sea ice, *Int. J. Remote Sensing*, 16 (17), 3343-3363, 1995.
- Cavalieri, D. J., P. Gloersen, and W. J. Campbell, Determination of sea ice parameters with the Nimbus-7 SMMR, *J. Geophys. Res.*, 89, 5355-5369, 1984.
- Comiso, J. C., and R. Kwok, Surface and radiative characteristics of the summer Arctic sea ice cover from multisensor satellite observations, *J. Geophys. Res.*, 101 (C12), 28,397-28,416, 1996.
- Hall, R. T., Seasonal photo mosaics of the AIDJEX triangle, *AIDJEX Bull.*, 39, 79-84, 1978.
- Hall, R. T., and D. A. Rothrock, Photogrammetric observations of the lateral melt of sea ice floes, *J. Geophys. Res.*, 92 (C7), pp. 7045-7048, 1987.
- Haverkamp, D., L. K. Soh, and C. Tsatsoulis, A comprehensive, automated approach to determining sea ice thickness from SAR data, *IEEE Trans. Geoscience and Remote Sensing*, 33, 46-57, 1995.
- Korsnes, R., Quantitative analysis of sea ice remote sensing imagery, *Int. J. Remote Sens.*, 14, 295-311, 1993.
- Martin, S., and R. Drucker, The effect of possible Taylor columns on the summer ice retreat in the Chukchi Sea, *J. Geophys. Res.*, 102 (C5), 10,473-10,482, 1997.
- Maslanik, J. A., M. C. Serreze, and R. G. Barry, Recent decreases in Arctic summer ice cover and linkages to atmospheric circulation anomalies, *Geophys. Res. Lett.*, 23 (13), 1677-1680, 1996.

- Maykut, G. A., and D. K. Perovich, The role of short-wave radiation in the summer decay of a sea ice cover, *J. Geophys. Res.*, 92, 7032-7044, 1987.
- Onstott, R. G., SAR and scatterometry signatures of sea ice, in *Microwave Remote Sensing of Sea Ice*, F. Carsey (ed.), Amer. Geophys. Union, Washington, DC, 73-104, Geophysical Monograph Series Vol. 68, 1992.
- Rothrock, D. A., and A. S. Thorndike, Measuring the sea ice floe size distribution, *J. Geophys. Res.*, 89, 6477-6486, 1984.
- Soh, L.-K., B. Holt, and C. Tsatsoulis, Identifying ice floes and computing ice floe distributions in SAR images, in *Analysis of SAR Data of the Polar Regions*, C. Tsatsoulis and R. Kwok (eds.), Springer-Verlag, New York, 9-34, 1998.
- Steele, M., Sea ice melting and floe geometry in a simple ice-ocean model, *J. Geophys. Res.*, 97 (C11), 17,729-17,738, 1992.
- Stoffelen, A., and D. Anderson, Scatterometer data interpretation: Derivation of the transfer function CMOD4, *J. Geophys. Res.*, 102 (C3), 5767-5780, 1997.
- Vinje, T. E., Sea Ice Studies in the Spitsbergen-Greenland area, NTIS Landsat Report E77-10206, 1977.
- Weeks, W. F., W. B. Tucker, M. Frank, and S. Fungcharoen, Characteristics of surface roughness and floe geometry of sea ice over the continental shelves of the Beaufort and Chukchi Seas, in *Sea Ice Processes and Models*, R. S. Pritchard (ed.), University of Washington Press, Seattle, 300-312, 1980.
- Winebrenner, D. P., E. D. Nelson, R. Colony, and R. D. West, Observation of melt onset on multiyear arctic sea ice using the ERS 1 synthetic aperture radar, *J. Geophys. Res.*, 99 (C11), 22,425-22,441, 1994.
- Winebrenner, D. P., B. Holt, and E. D. Nelson, Observations of autumn freeze-up in the Beaufort and Chukchi Seas using the ERS-1 synthetic aperture radar, *J. Geophys. Res.*, 101(C7), 16,401-16,419, 1996.

Table 1. ERS-1 SAR data used in the analysis. DOY stands for Day of Year.

Orbit No.	Start Center Lat°N/Lon°W	End Center Lat°N/Lon°W	DOY UT	Day in Aug	Total frames No.	Good Floe Images (No.)		
						72-75°	75-78°	78-83°
Beaufort								
5642	77.3/143.1	71.4/152.8	226:21:49	13	9	4	4	0
5685	80.3/134.2	71.1/154.6	229:21:55	16	14	2	3	1
5728	82.3/123.0	71.5/155.7	232:22:01	19	17	2	4	5
5814	82.9/120.3	71.6/158.5	238:22:12	25	18	0	4	8
5828	82.0/120.3	71.1/151.1	239:21:41	26	17	2	3	4
Chukchi								
5571	76.1/160.0	72.5/165.8	221:22:47	08	6	2	2	0
5614	80.1/149.8	71.6/168.5	224:22:52	11	9	1	2	0
5657	82.3/137.8	71.4/170.1	227:22:00	14	17	2	4	5
5700	80.2/151.9	71.8/171.2	230:23:04	17	13	0	3	4
5743	82.4/139.8	72.3/172.0	233:23:09	20	16	0	1	3
5800	79.2/151.2	72.7/164.9	237:22:44	24	10	0	2	2
5829	81.8/150.8	72.3/174.9	239:23:21	26	14	1	2	5
Wrangel								
5643	78.1/165.9	71.6/177.8	226:23:30	13	10	0	3	1
5672	78.1/175.3	75.3/178.3E	229:00:07	16	5	0	0	0
5772	78.3/169.9	72.5/179.0E	235:23:47	22	9	0	2	1
Total Frames					184	16	39	39

Table 2. Definition of the floe size classes. See text for additional description.

Class	PixelRange	Mean Area	Mean Area	Mean d
No.		(Pixels)	(km ²)	(km)
1	1	1	0.01	0.12
2	2	2	0.02	0.15
3	3-4	3.5	0.04	0.23
4	5-8	6.5	0.07	0.31
5	9-16	13	0.1	0.44
6	17-32	25	0.3	0.61
7	33-64	49	0.5	0.86
8	65-130	97	1.0	1.2
9	130-260	1.9×10^2	1.9	1.7
10	260-510	3.8×10^2	3.8	2.4
11	$510-1.0 \times 10^3$	7.7×10^2	8	3.4
12	$1.0-2.0 \times 10^3$	1.5×10^3	15	5
13	$2.0-4.1 \times 10^3$	3.1×10^3	31	7
14	$4.1-8.2 \times 10^3$	6.1×10^3	60	10
15	$8.2-16 \times 10^3$	1.2×10^4	120	14
16	$>1.6 \times 10^4$	2.5×10^4	250	19

Table 3. Observed slopes as a function of latitude bands for the three swaths. The least squares are done for a floe size range of class 7 to 14, or a diameter range of 0.9 to 10 km. See text for further description.

Latitude band\swath (°N)	Wrangel	Chukchi	Beaufort
78-83	2.4 ± 0.1	2.3 ± 0.1	1.9 ± 0.05
75-78	2.5 ± 0.2	2.2 ± 0.1	1.9 ± 0.05
72-75	-	2.6 ± 0.3	2.2 ± 0.07
72-83	2.5 ± 0.1	2.4 ± 0.1	2.0 ± 0.05
72-78	2.5 ± 0.2	2.4 ± 0.15	2.1 ± 0.05

Figure Captions

Figure 1. Chart of the study region showing the approximate locations of the ERS-1 SAR swaths, labeled "Beaufort", "Chukchi" and "Wrangel". The shaded regions bound the locations of the 100-km wide individual swaths used in the analysis.

Figure 2. The daily geostrophic wind measured at 72.5°N, 168.0°W, for the period June - September 1992. The upper arrows show the direction in which the wind is blowing; the lower bars show the wind magnitude in m s^{-1} .

Figure 3. The sequence of surface pressure charts for 00 Z, 7 - 21 August 1992. The latitude/longitude lines are at 5° intervals.

Figure 4. The SSM/I-derived ice edge for Beaufort, Chukchi and East Siberian Seas. The continents are black, the gray-scale lines show the ice edge position as derived from three-day SSM/I averages. The black rectangle outlines a region to be used in our SAR discussion; the winds shown in Figure 2 are calculated close to the center of this rectangle.

Figure 5. Geolocated SAR images of the Chukchi Sea ice edge. The boundaries of each image correspond to the rectangle shown in Figure 4; the letters X, Y identify features common to pairs of images. (5a) 8 August, (5b) 11 August, (5c) 14 August, (5d) 17 August, (5e) 20 August. Images copyright ESA 1992.

Figure 6. The summer dependence of the C-Band VV radar backscatter. The dashed lines show the open water backscatter at two different wind speeds; the solid lines show the backscatter range for sea ice. See text for further description.

Figure 7. An example of (7a) an ERS-1 SAR image, without slope correction, (7b) floe size distribution, (7c) the percentage of the four derived outputs, and (7d) the fractional area percent of each derived floe size class. Note that in (7b) open water is white and substrate is gray which matches the color labeled substrate in (7c). See text for further description. Image copyright ESA 1992.

Figure 8. Changes with time in the ice concentration for the three swaths. (8a) Wrangel, (8b) Chukchi, (8c) Beaufort. See text for further description.

Figure 9. The number of floes versus floe size class and for the three different latitude bands, averaged for the periods 8-13 August, 14-20 August, and 21-26 August. (9a) Wrangel, (9b) Chukchi, (9c) Beaufort. See text for further description.

Figure 10. The areal floe coverage versus floe class and for the three different latitude bands, averaged for the periods 8-13 August, 14-20 August, and 21-26 August. (10a) Wrangel, (10b) Chukchi, (10c) Beaufort. Note that in (10c) upper panel, the area for class 16 is 1,500 km². See text for further description.

Figure 11. The cumulative number of floes for each swath versus the three latitude bands and for the periods 8-13 August, 14-20 August, and 21-26 August. See text for additional description

Figure 12. The cumulative number of floes versus floe diameter. (12a) A redrawn version of Figure 7 from *RT-84*; (12b) Floe size results for each swath superimposed onto the *RT-84* results, where we have plotted the mean of all values between 0.9 and 10 km (classes 7-14) and between 72-78°N. See text for additional description.

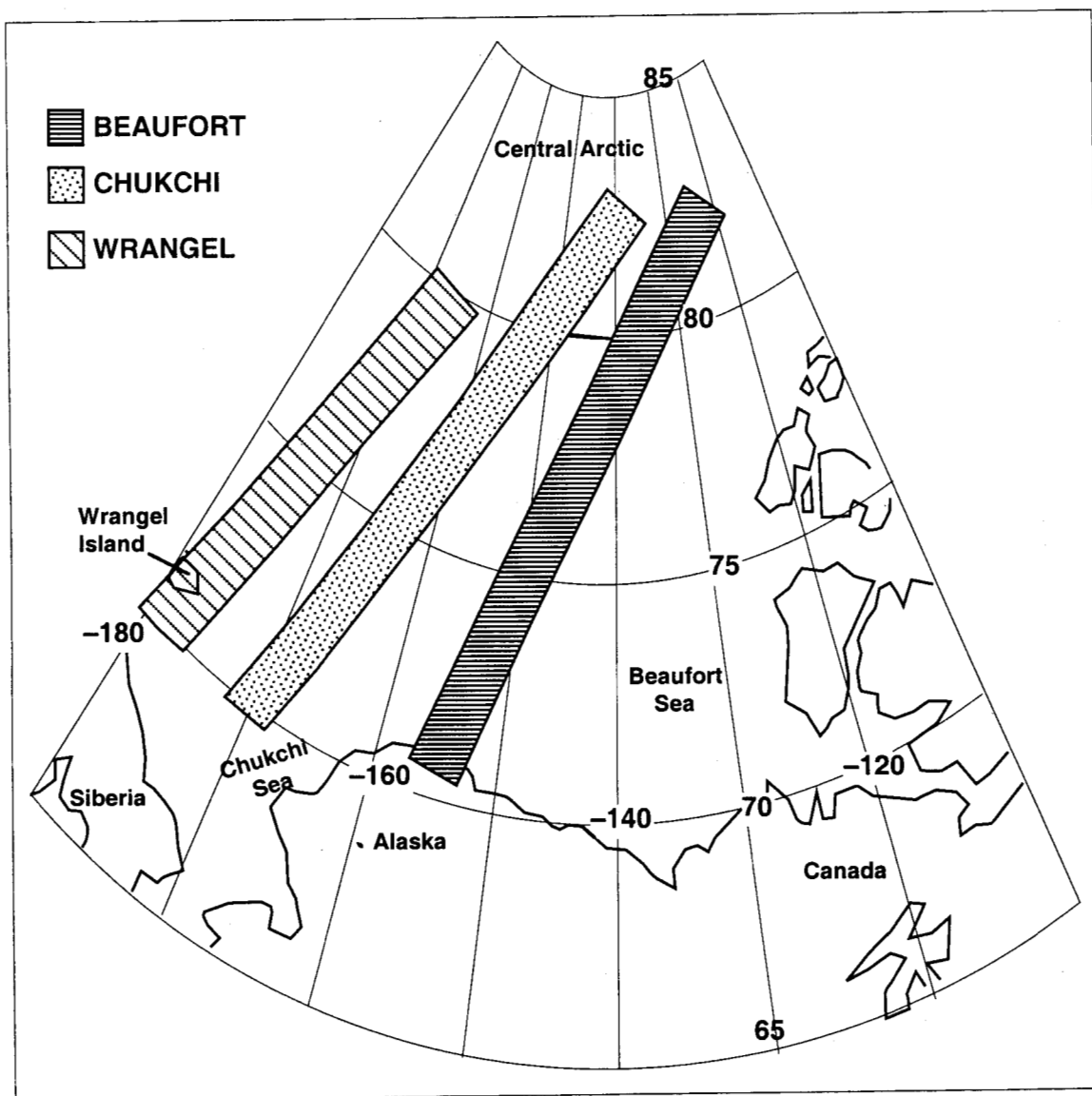


Fig. 1

Geostrophic wind at 72.50N, 168.00W (1992)

Up is north; dials point away from the wind.

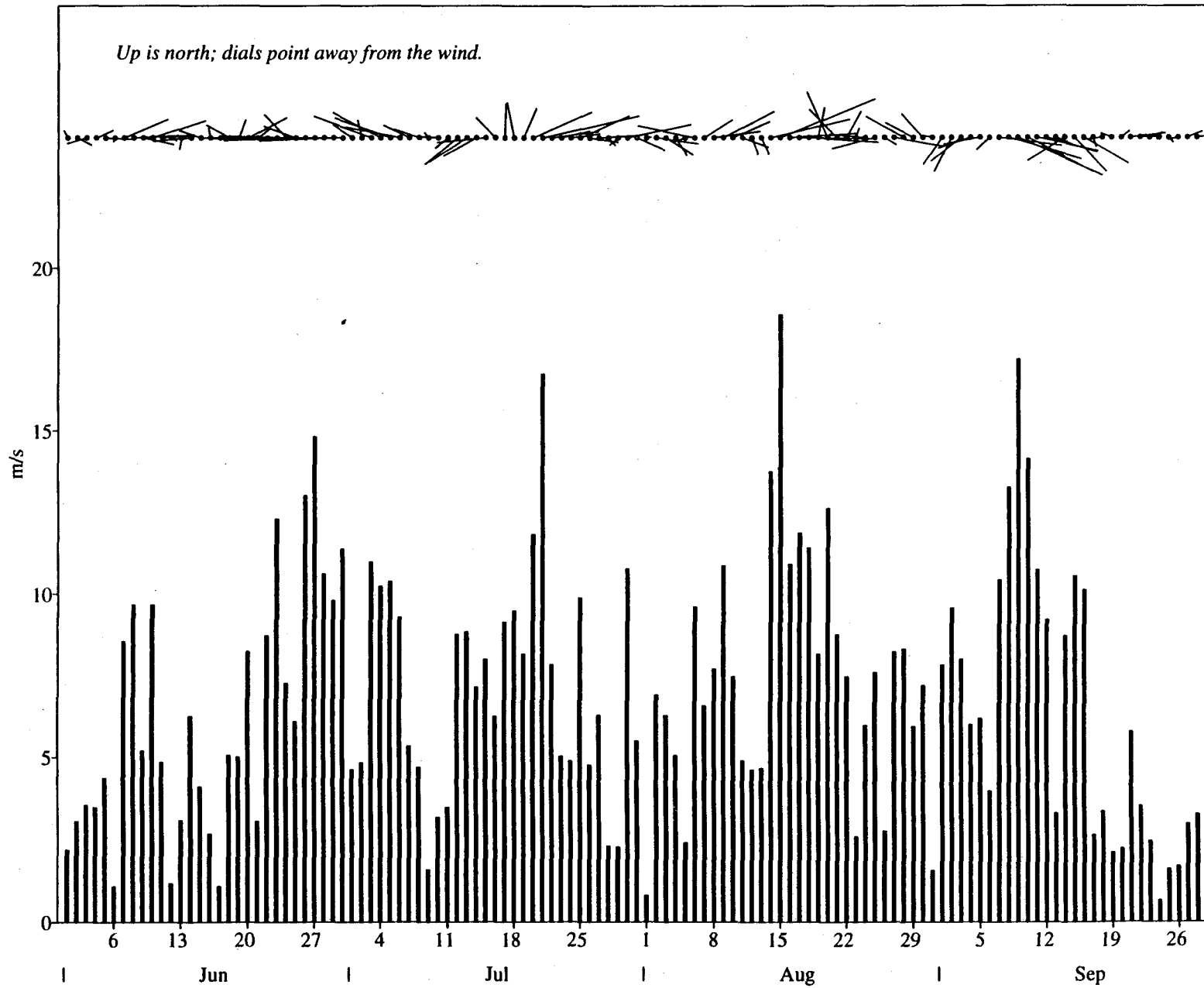


Fig. 2

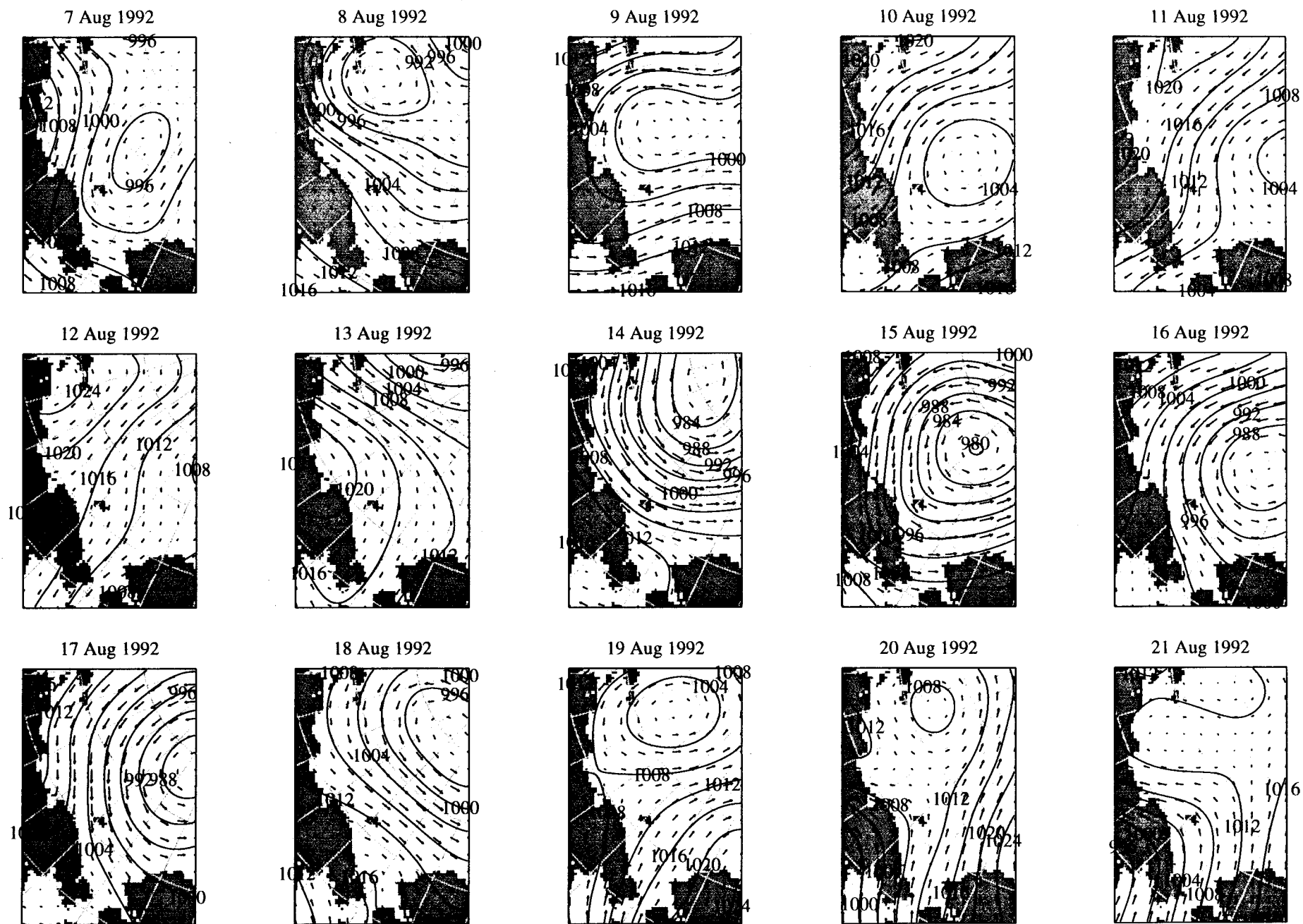


Fig 3

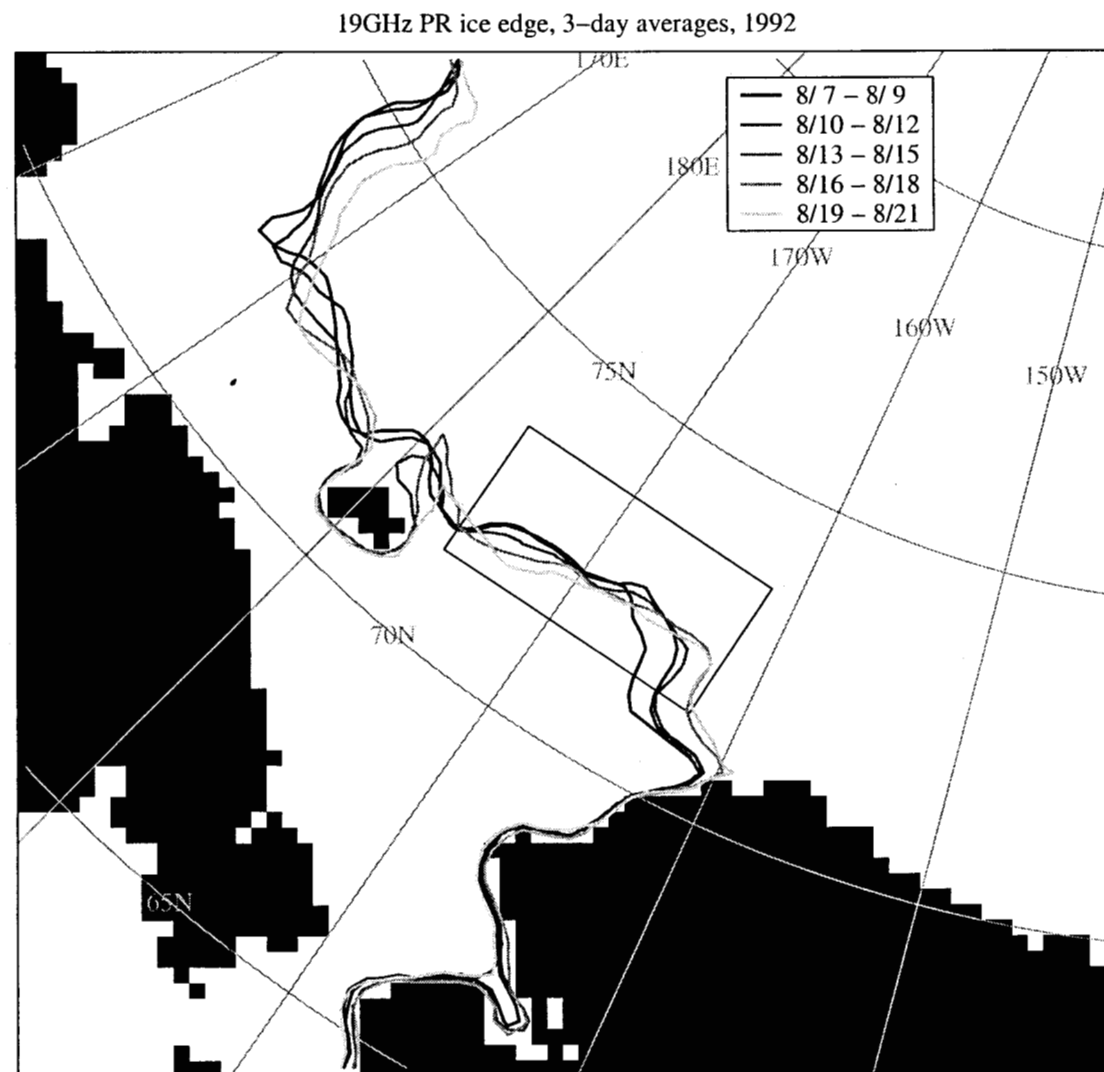
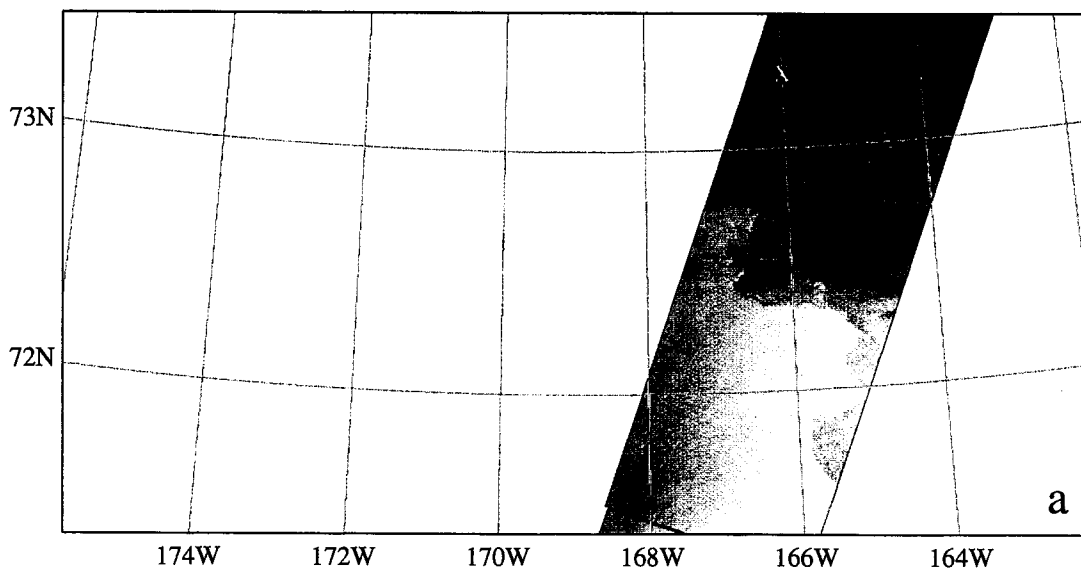
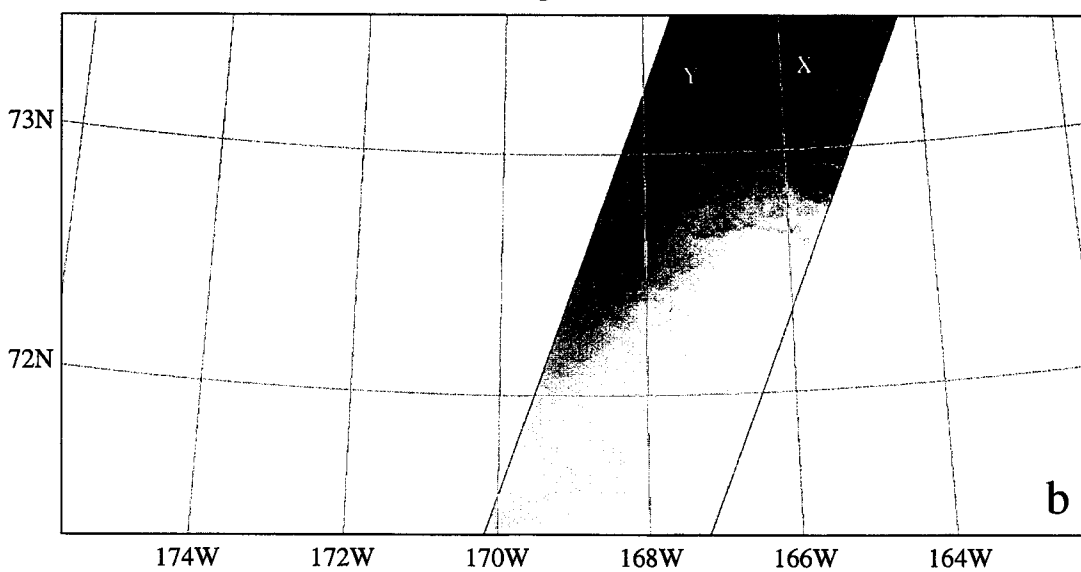


Fig 4

Aug 8 1992



Aug 11 1992



Aug 14 1992

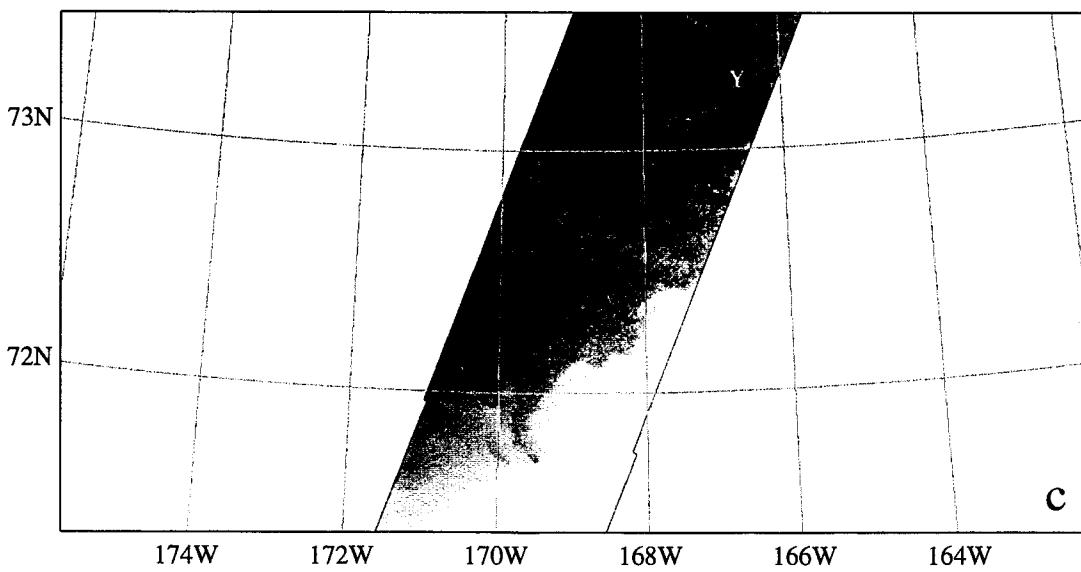
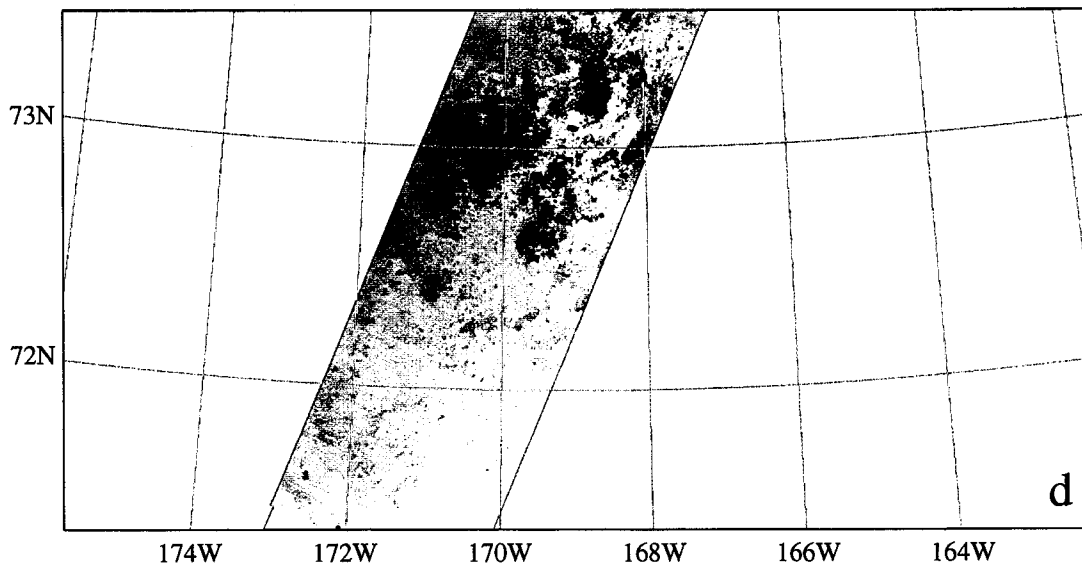


Fig 5a

Aug 17 1992



Aug 20 1992

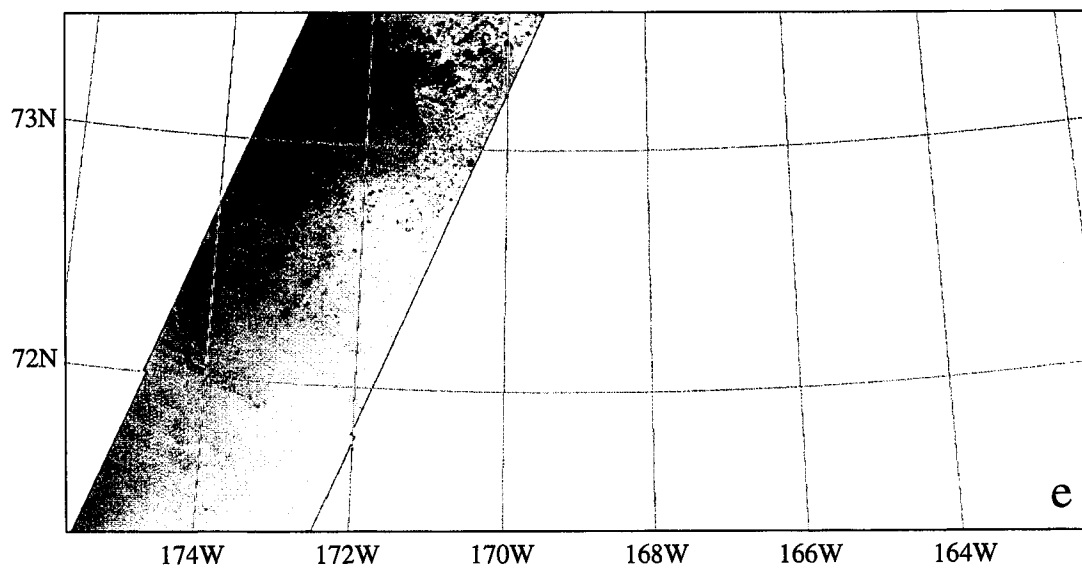


Fig 5 b

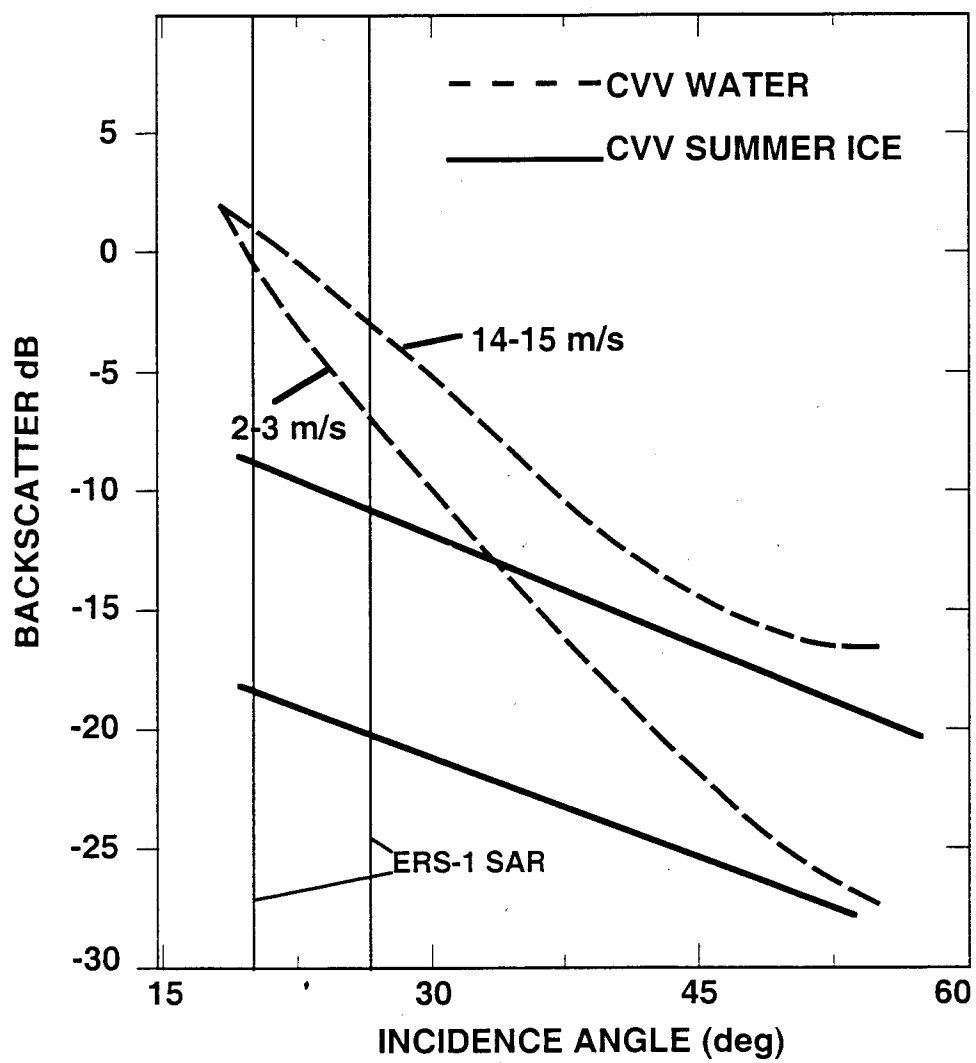


Fig 6

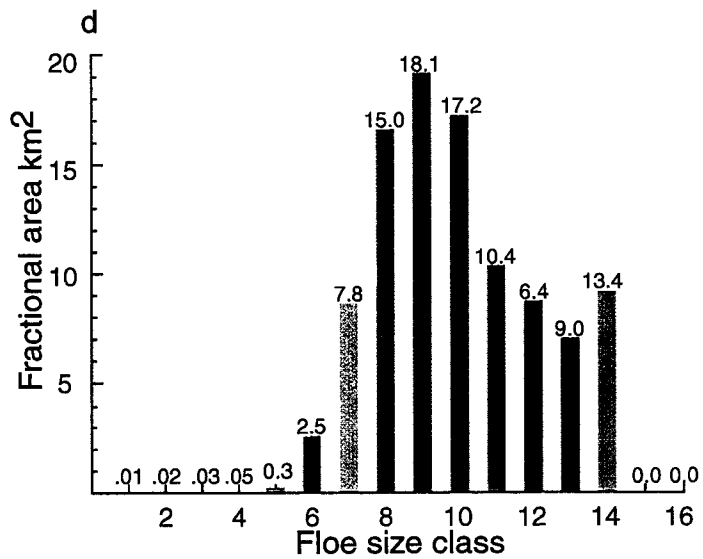
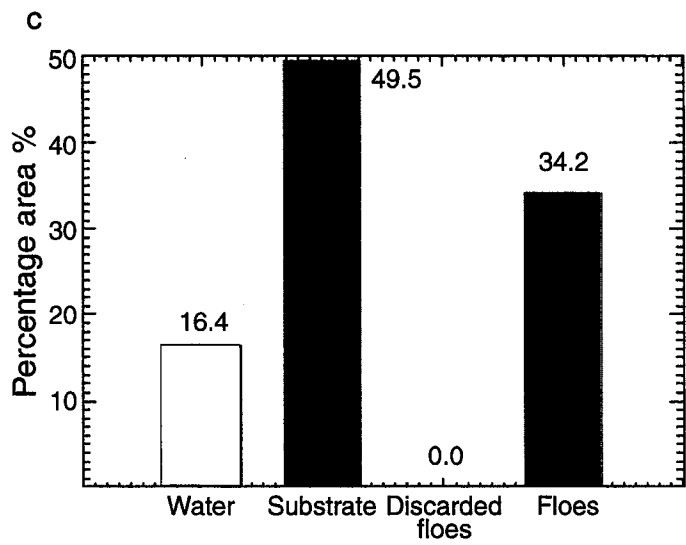
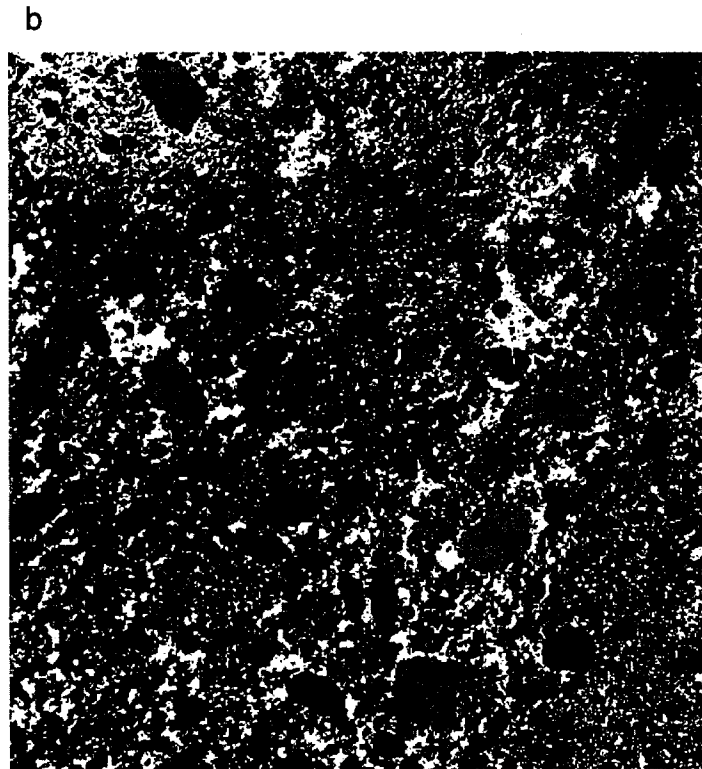
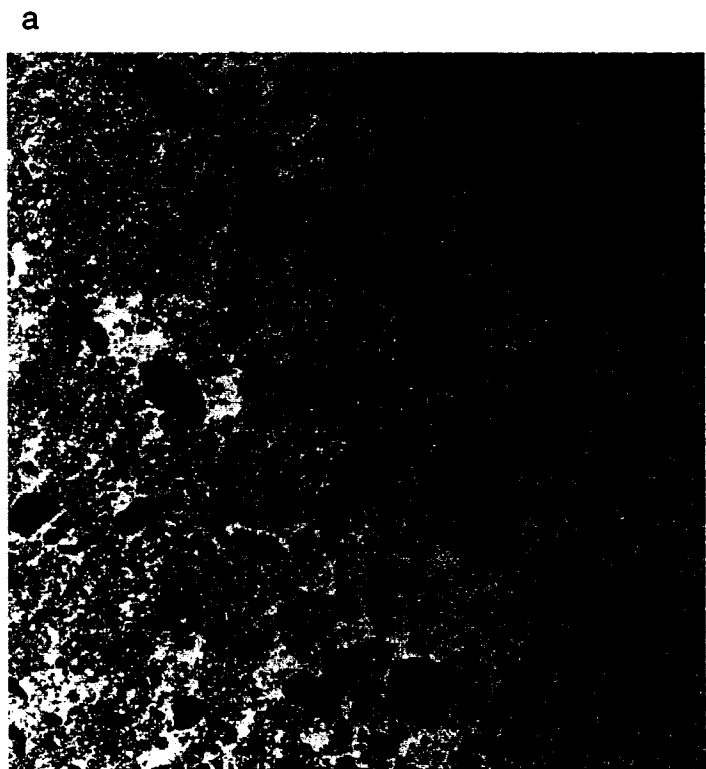


Fig 7

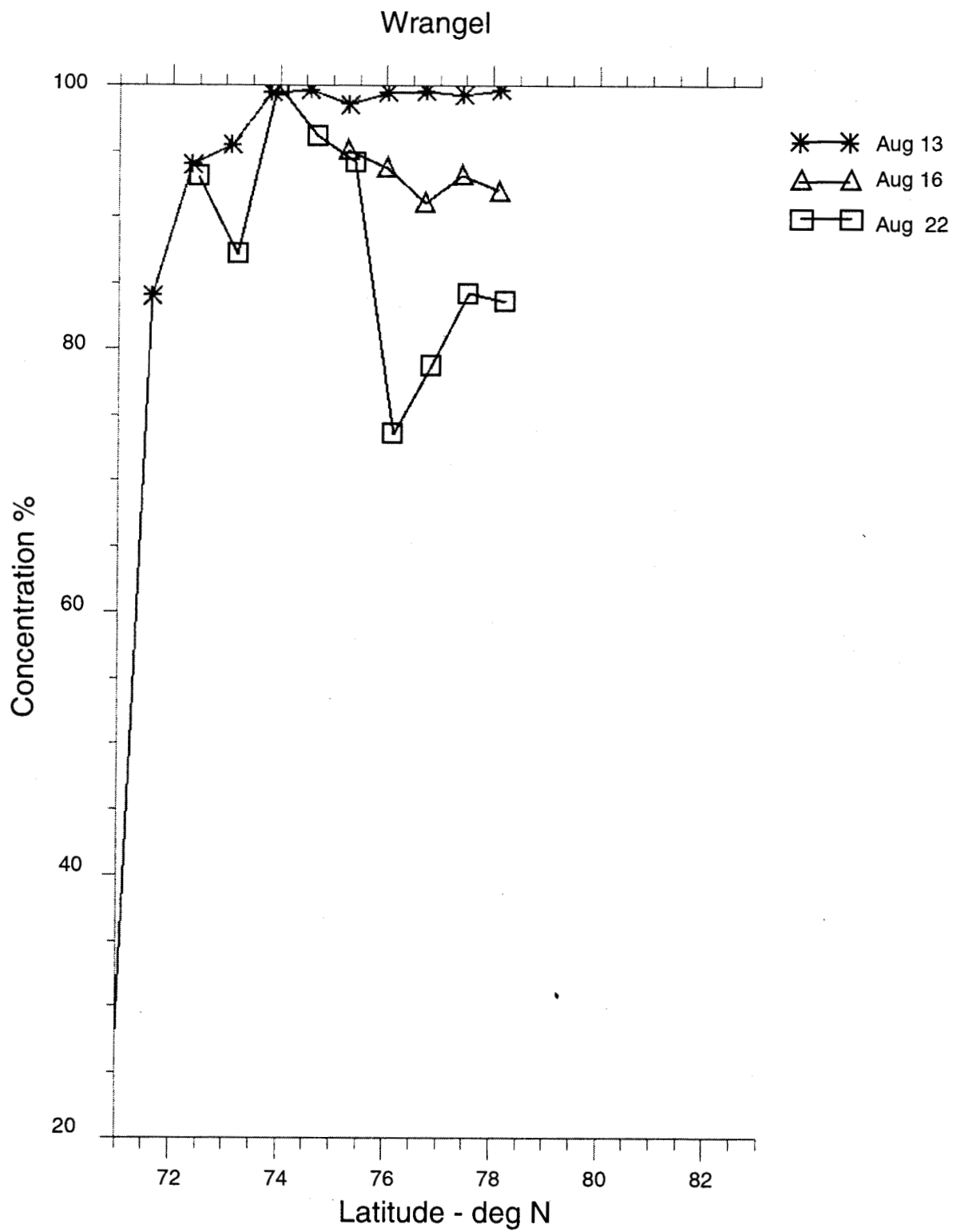


Fig 8a

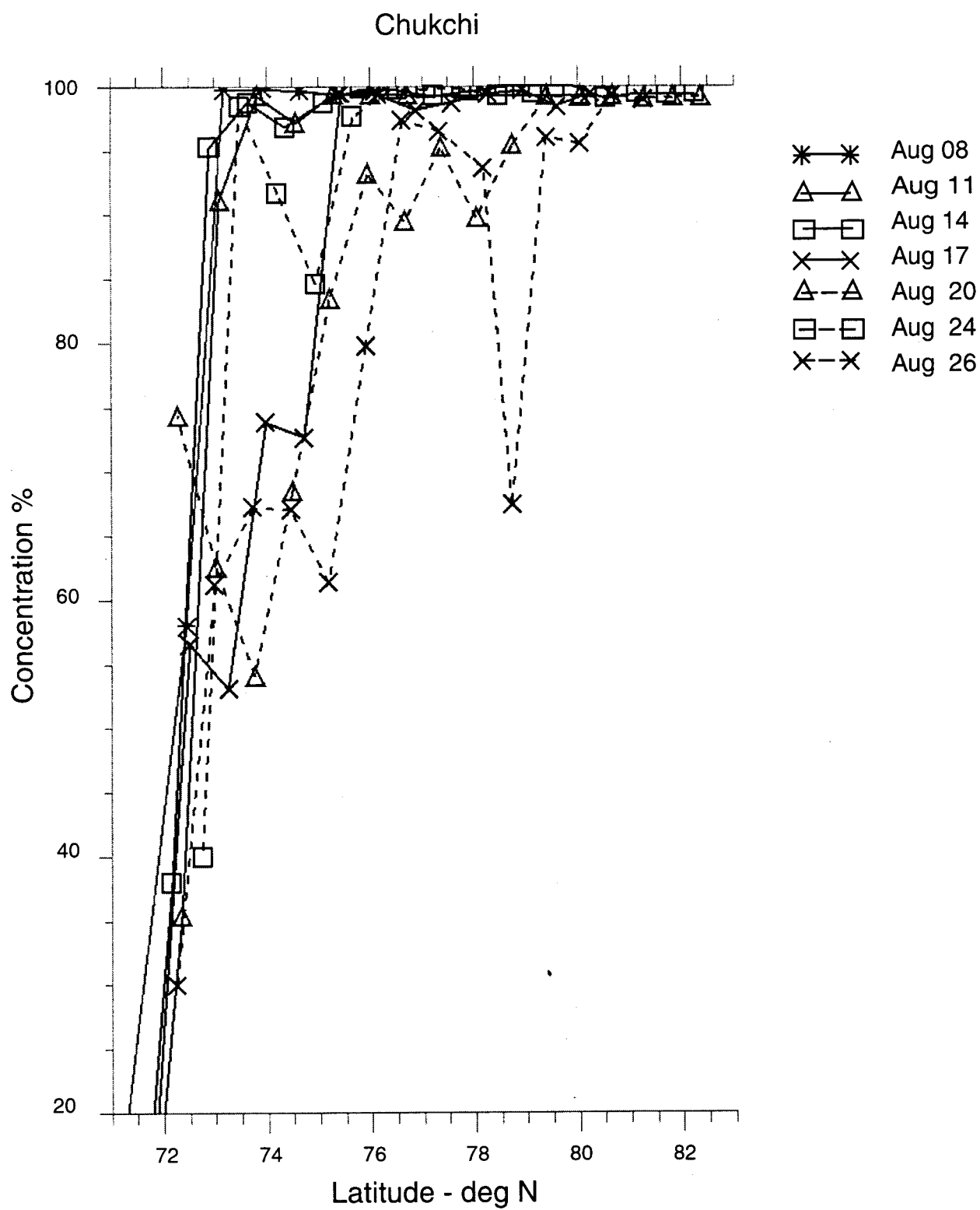


Fig 8b

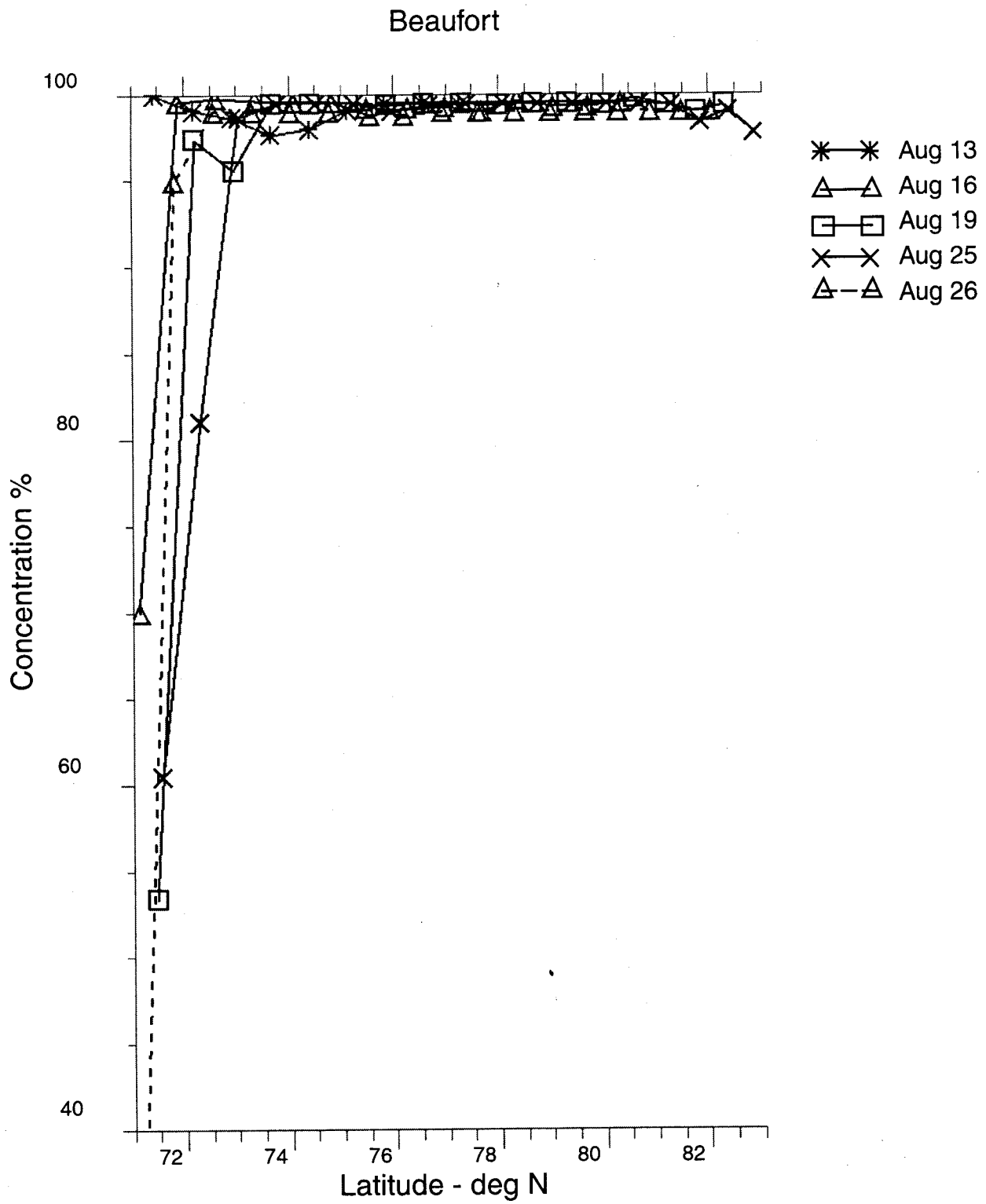


Fig 8c

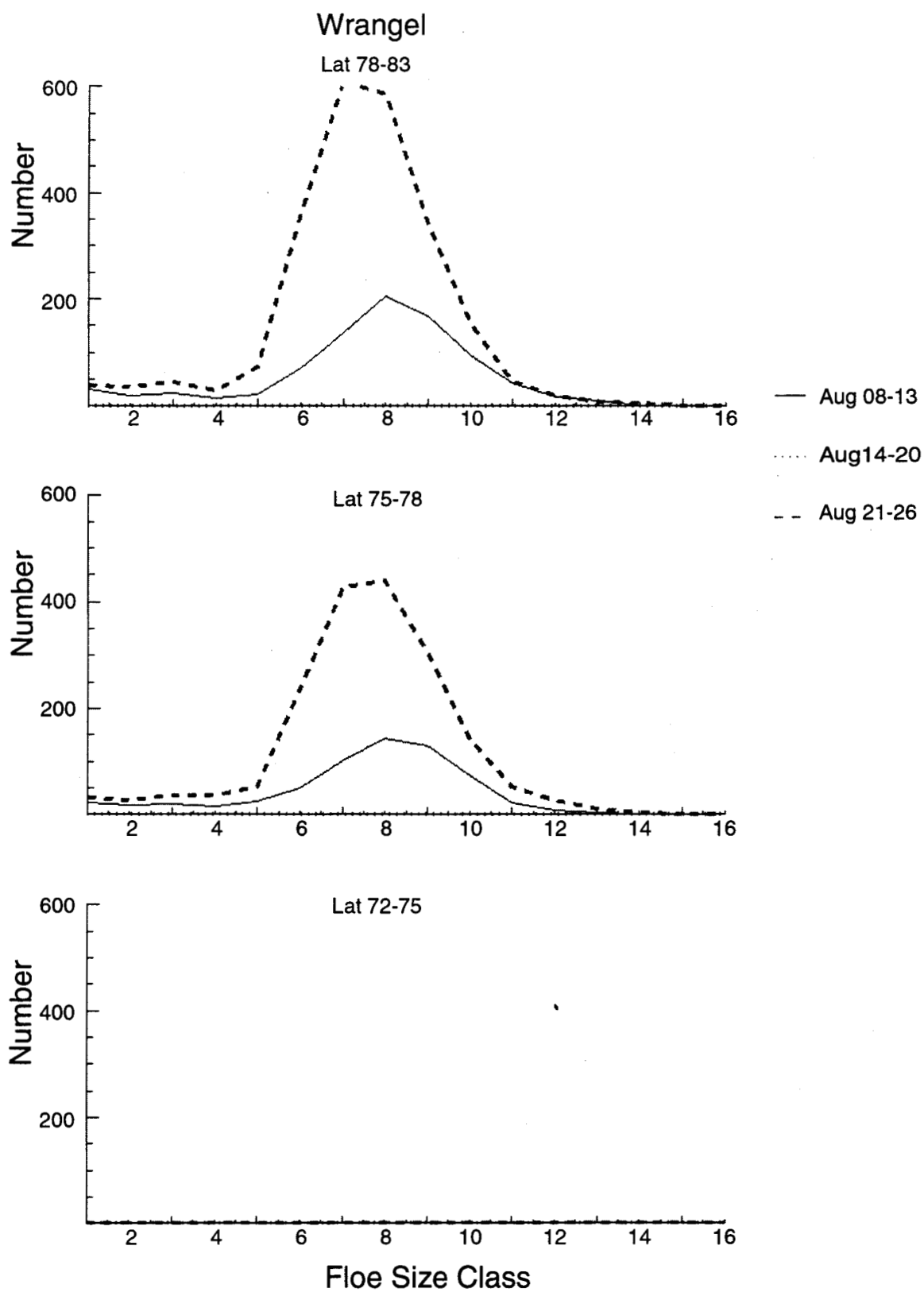


Fig 9a

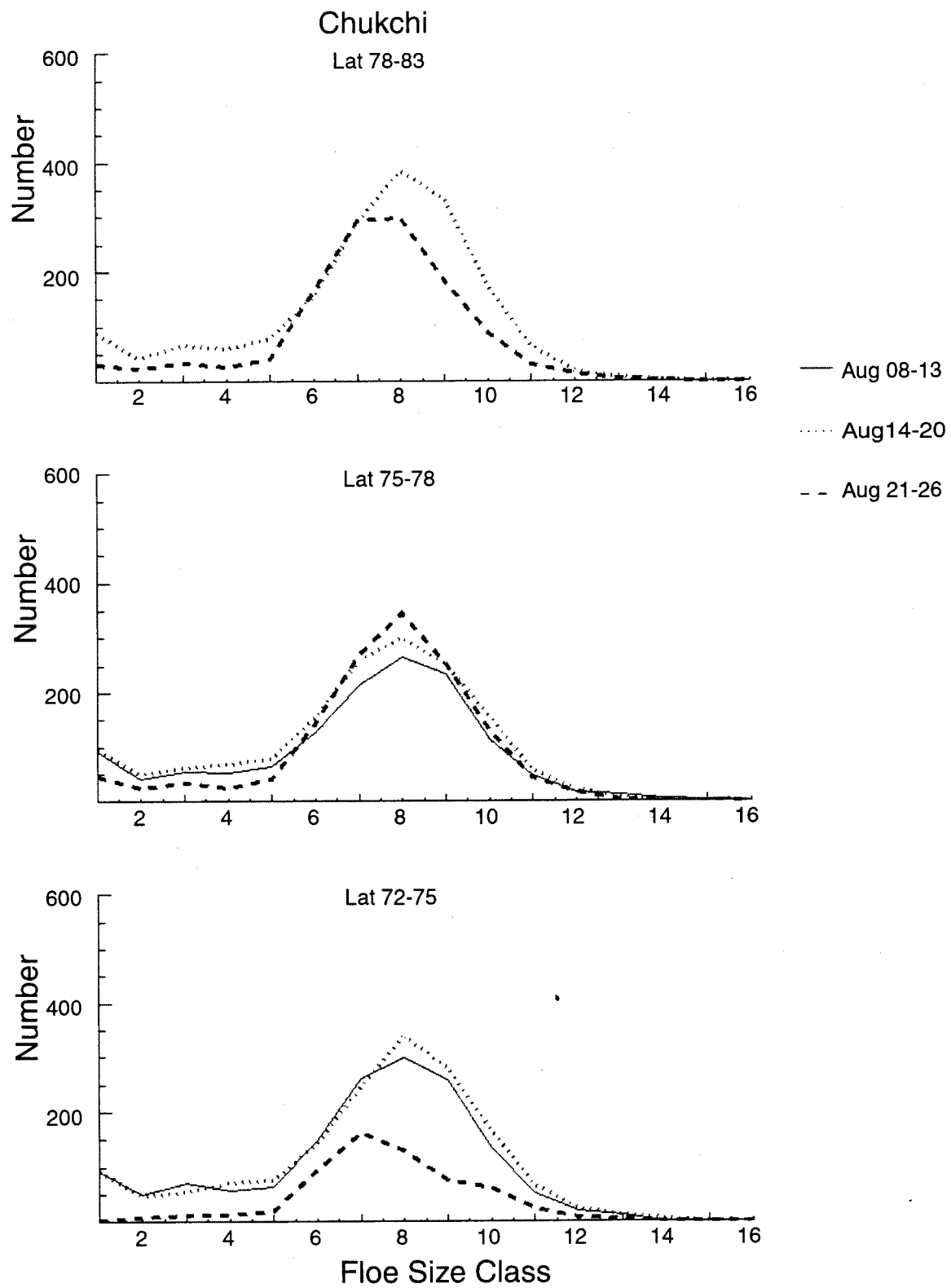


Fig 9b

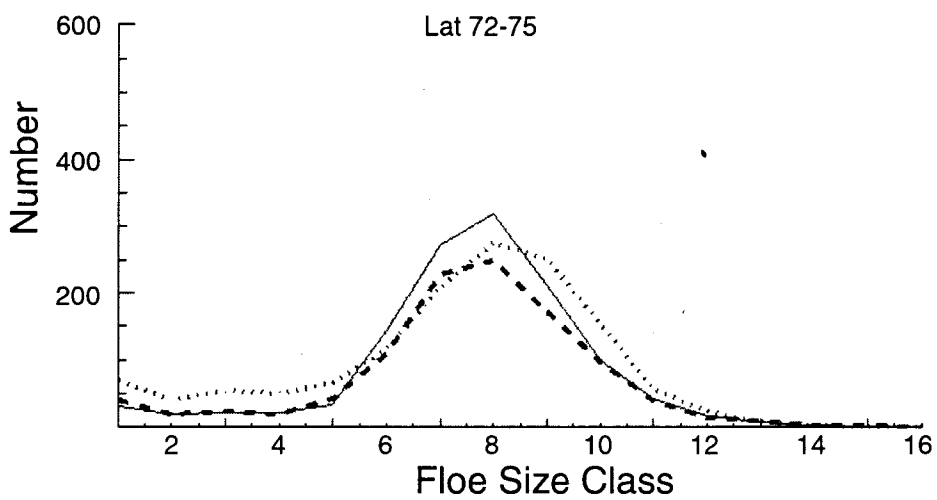
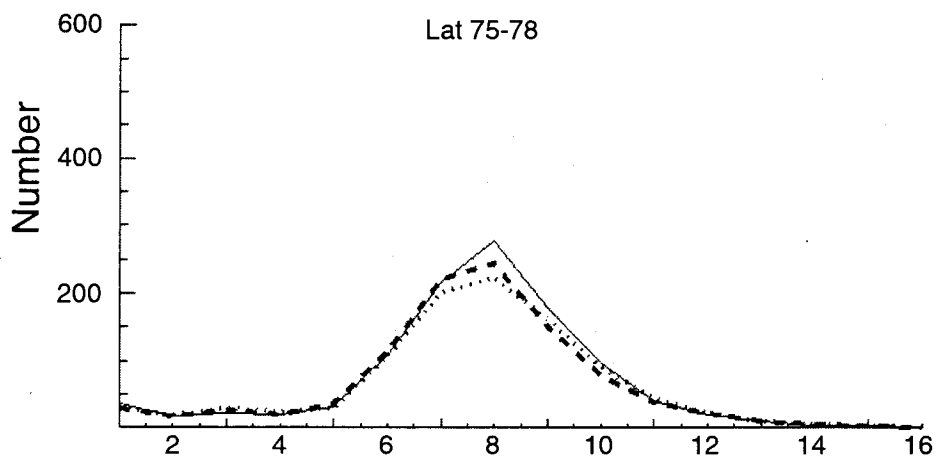
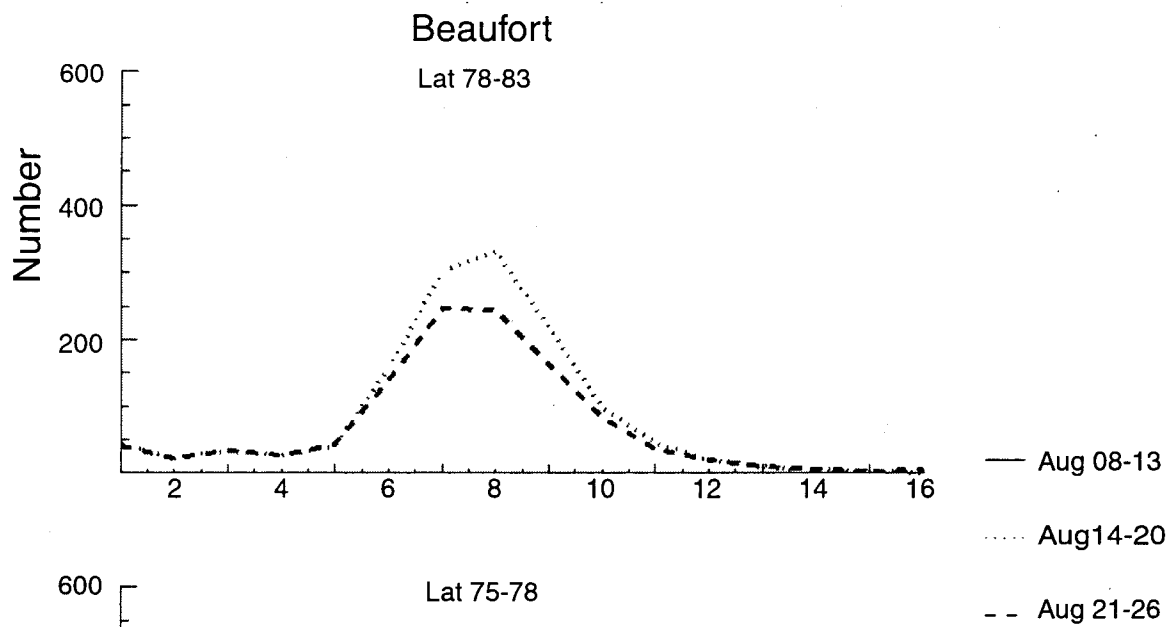


Fig 9c

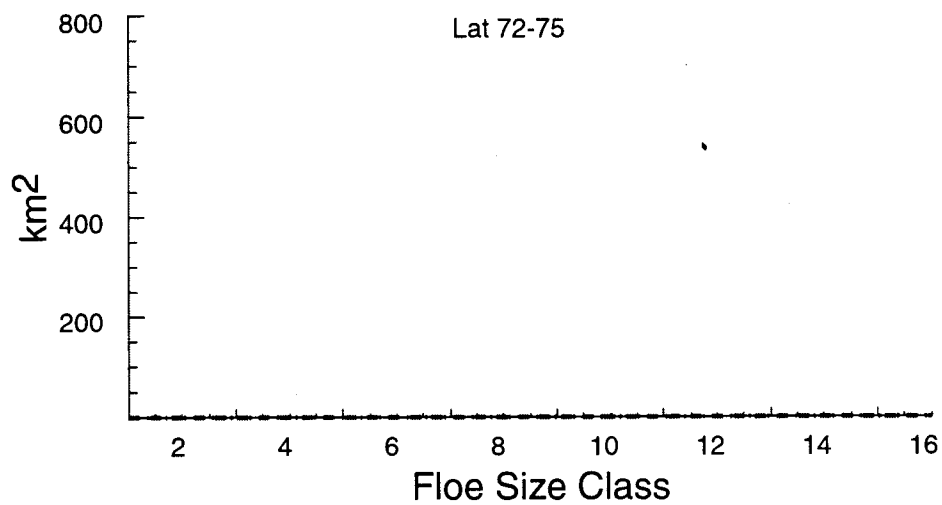
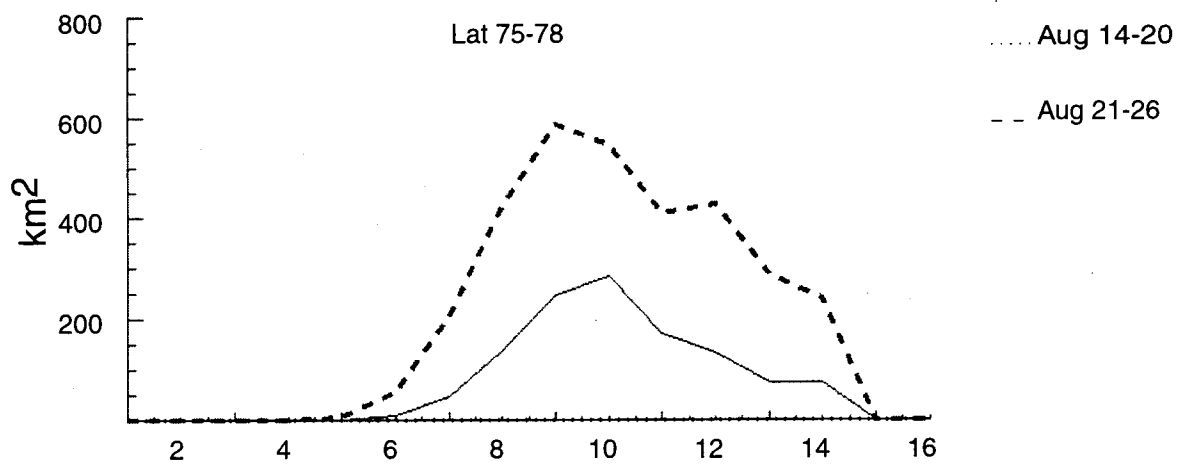
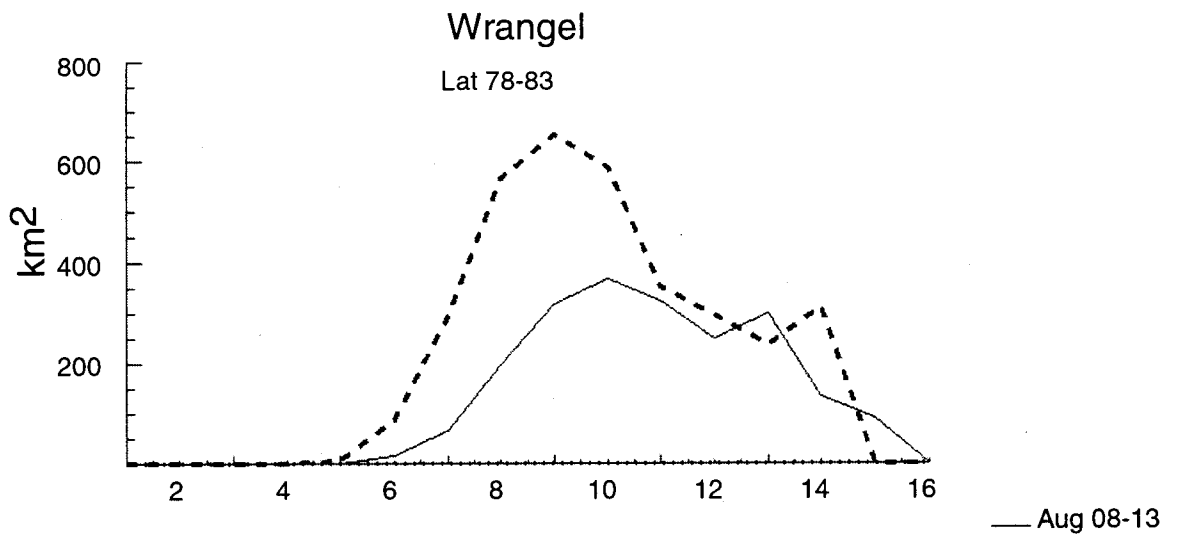


Fig 10a

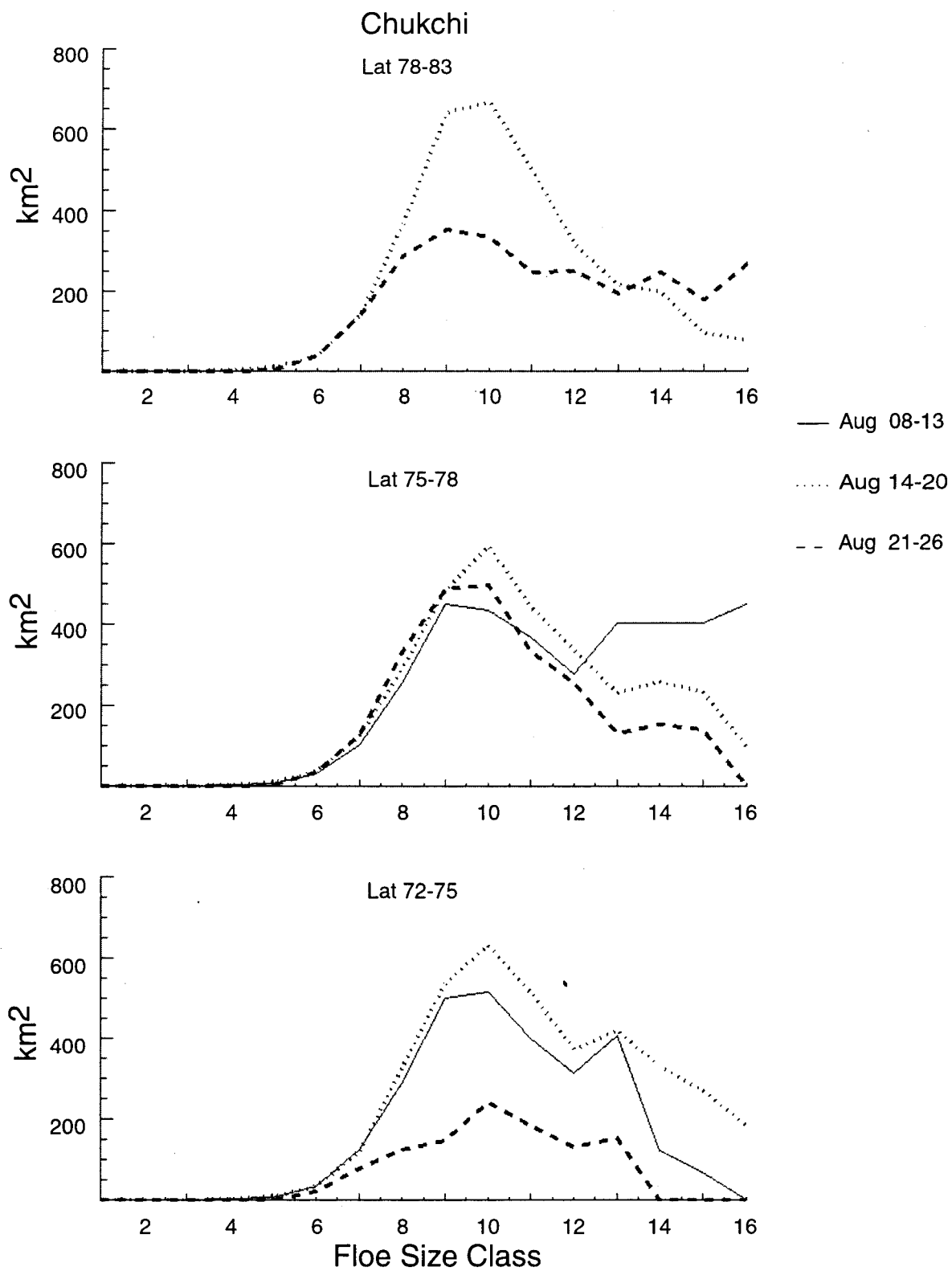


Fig 10b

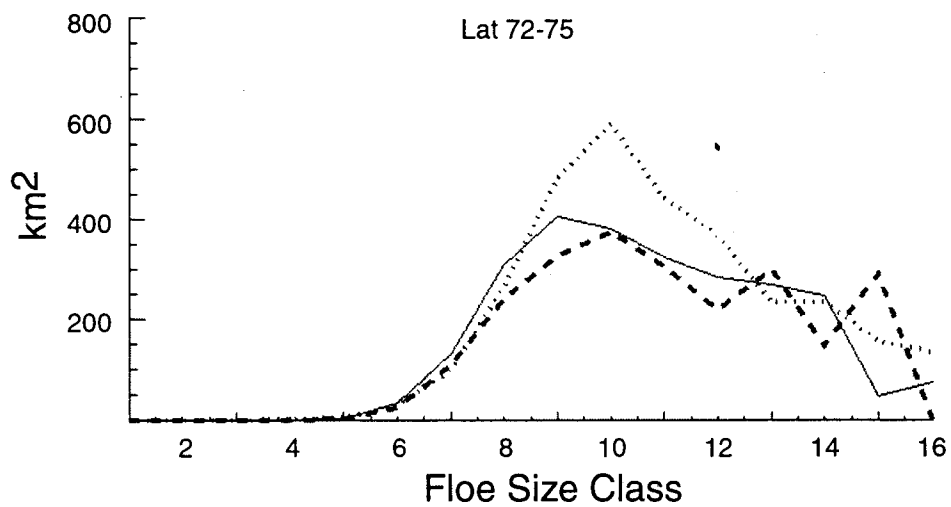
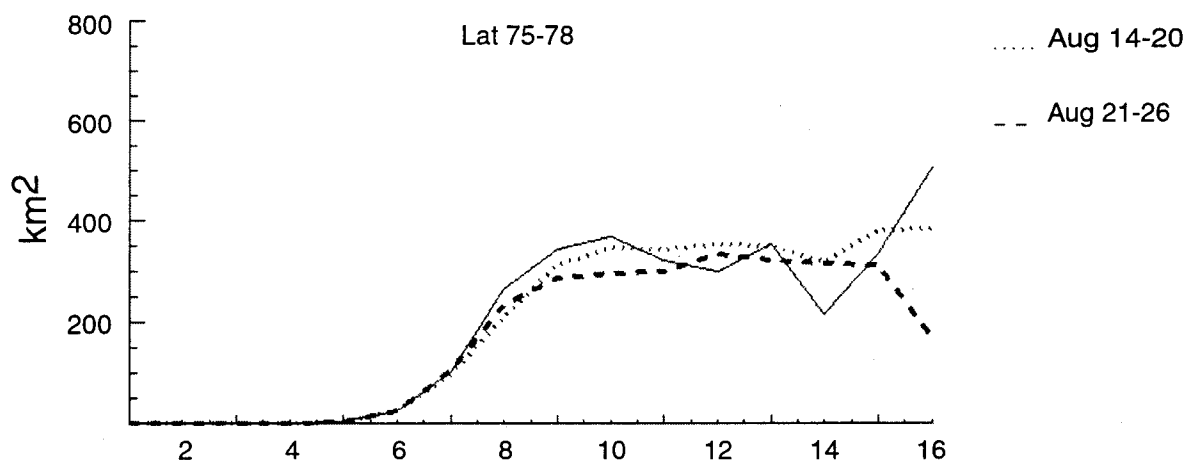
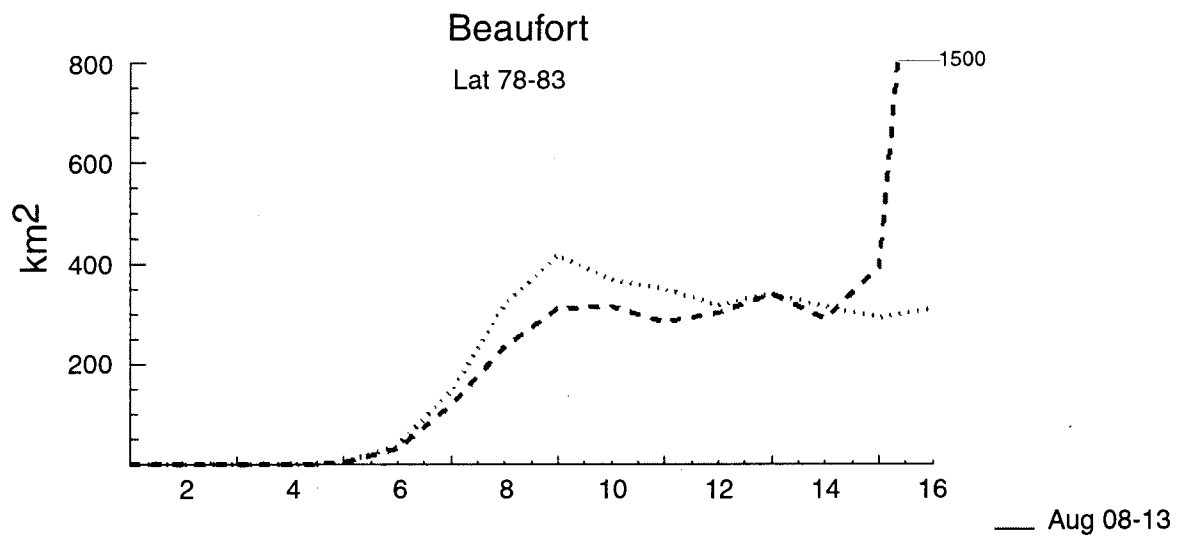


Fig 10c

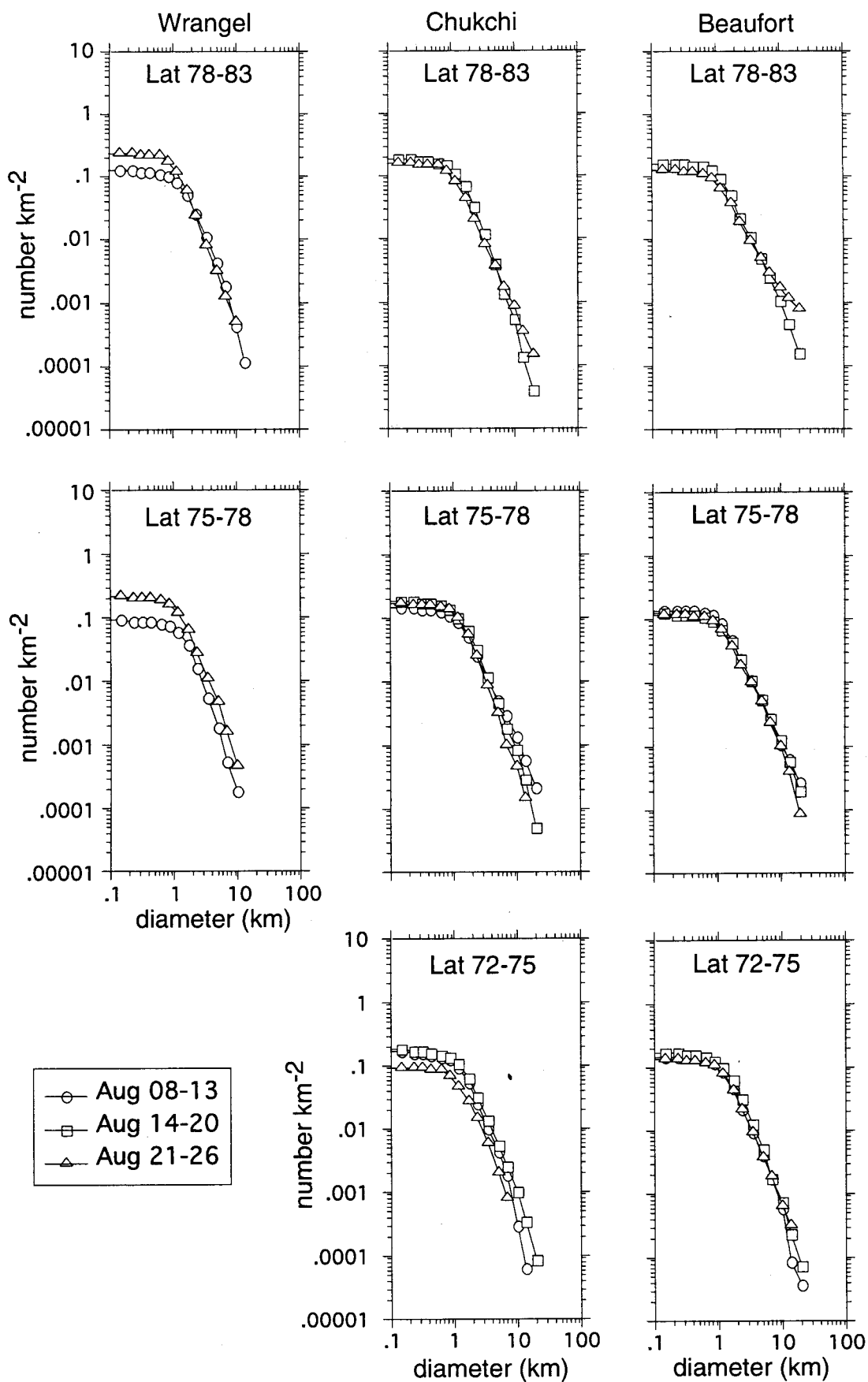


Fig 11

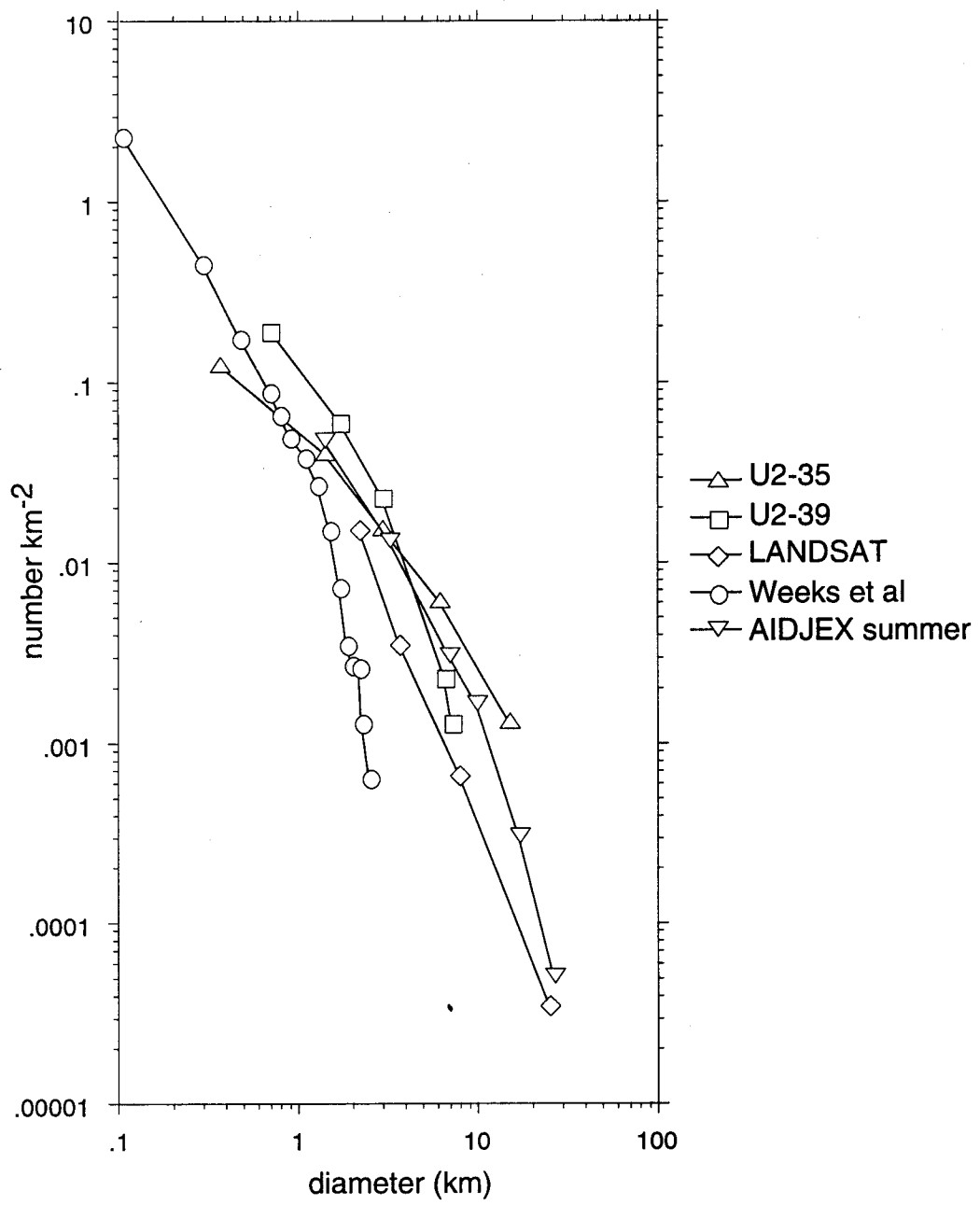


Fig 12a

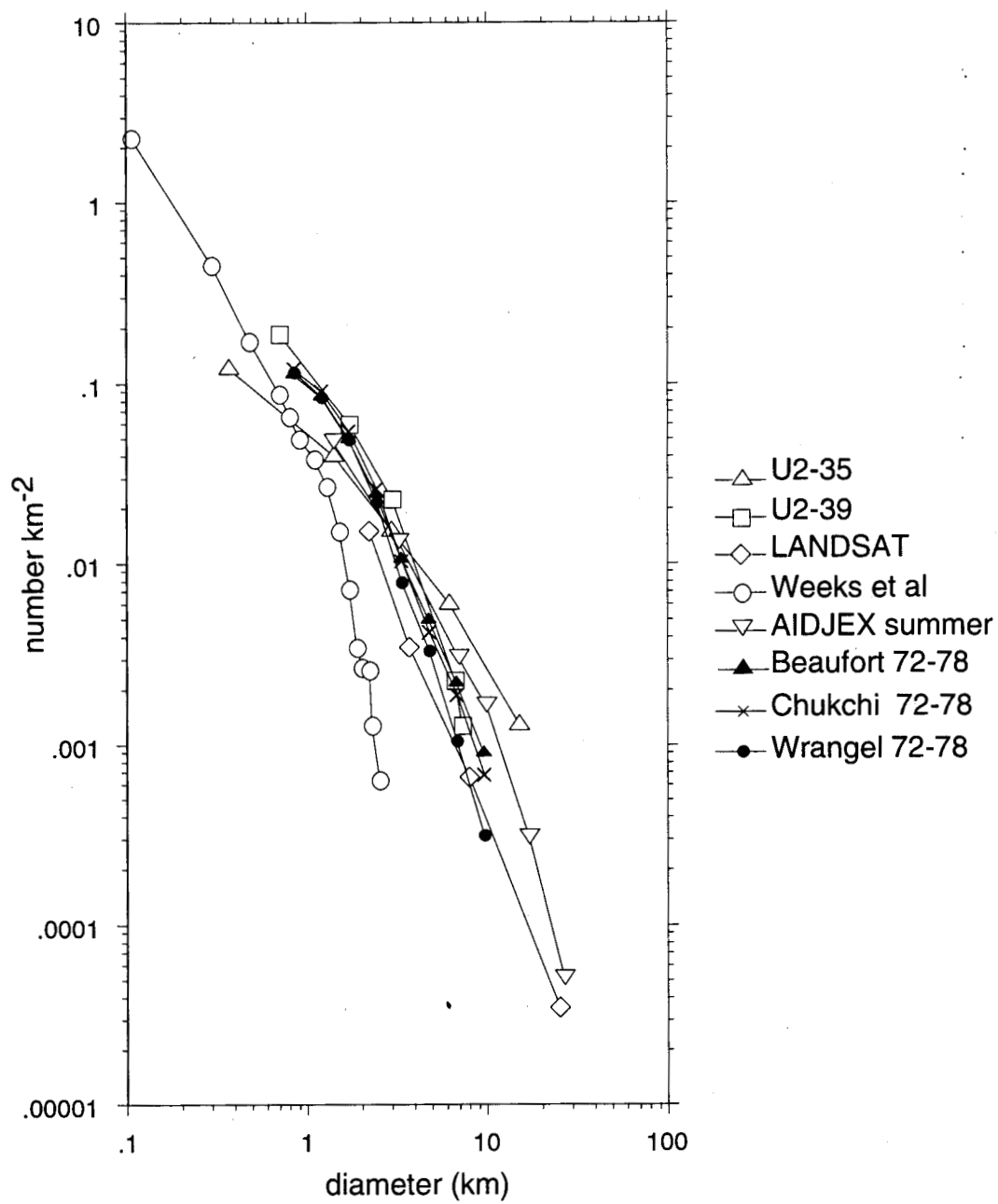


Fig 126